nature communications

Article

https://doi.org/10.1038/s41467-025-61653-w

Anisotropic spin stripe domains in bilayer $La_3Ni_2O_7$

Received: 1 November 2024

Accepted: 27 June 2025

Published online: 16 July 2025

Check for updates

Naman K. Gupta[1,8], Rantong Gong[1,8], Yi Wu[2,8], Mingu Kang[2,3,4], Christopher T. Parzyck[2], Benjamin Z. Gregory[2,3], Noah Costa[1], Ronny Sutarto[5], Suchismita Sarker[6], Andrej Singer[3], Darrell G. Schlom[3,4,7], Kyle M. Shen[2,4] ✉ & David G. Hawthorn[1] ✉

The discovery of superconductivity in $La_3Ni_2O_7$ under pressure has motivated the investigation of a parent spin density wave (SDW) state, which could provide the underlying pairing interaction. Here, we employ resonant soft x-ray scattering and polarimetry on thin films of bilayer $La_3Ni_2O_7$ to determine that the magnetic structure of the SDW forms unidirectional diagonal spin stripes with moments lying within the NiO_2 plane and perpendicular to Q_{SDW}, but without evidence of the strong charge disproportionation typically associated with other nickelates. These stripes form anisotropic domains with shorter correlation lengths perpendicular versus parallel to Q_{SDW}, revealing nanoscale rotational and translational symmetry breaking analogous to the cuprate and Fe-based superconductors, with possible Bloch-like antiferromagnetic domain walls separating orthogonal domains.

The discovery of superconductivity with a transition temperature (T_c) above 80 K under hydrostatic pressure has ignited intense interest in $La_3Ni_2O_7$[1] as a new platform to compare against the Cu- and Fe-based superconductors to understand which common ingredients are essential for realizing high T_c's[2,3]. In both the cuprates and Fe-based families, parent antiferromagnetic states as well as nematicity are both known to play critical roles in their phase diagrams, the detailed understandings of which are essential for developing microscopic models. Presently, our understanding of the parent state from which the superconductivity condenses in $La_3Ni_2O_7$ remains incomplete. Recent resonant inelastic x-ray scattering (RIXS)[4], heat capacity and magnetic susceptibility[5,6], nuclear magnetic resonance (NMR)[7,8] and μSR[9,10] measurements of bulk $La_3Ni_2O_7$ suggest the presence of a spin density wave (SDW) transition occurring around $T_{SDW} \approx 150$ K, with a wavevector of $(H = \frac{1}{4}, K = \frac{1}{4})$ deduced from RIXS[4]. However, essential information regarding the microscopic spin structure and orientation remains unresolved.

Here, we present detailed resonant soft x-ray scattering (RSXS) and polarimetry measurements on epitaxial thin films of bilayer $La_3Ni_2O_7$, which reveal that the detailed spin structure consists of equal domains of bicollinear spin stripes, with the spins lying in the NiO_2 plane and aligned perpendicular to the SDW wavevector. Temperature-dependent spectroscopic measurements support a scenario with only a single electronic Ni site, with no evidence for charge or bond disproportionation across T_{SDW}, and where the oxygen ligand holes are strongly hybridized with the Ni d orbitals. The SDW domains exhibit a surprising anisotropy in their correlation lengths parallel versus perpendicular to their wavevector, suggesting that nanoscale rotational symmetry breaking might also play an important role in $La_3Ni_2O_7$, reminiscent of the nematic order found in the cuprates and Fe-based superconductors[11–13]. Finally, a detailed polarization and temperature-dependent analysis of the SDW Bragg peaks suggests the presence of extended, Bloch-like domain walls between orthogonal domains.

[1]Department of Physics and Astronomy, University of Waterloo, Waterloo, Canada. [2]Laboratory of Atomic and Solid State Physics, Department of Physics, Cornell University, Ithaca, NY, USA. [3]Department of Materials Science and Engineering, Cornell University, Ithaca, NY, USA. [4]Kavli Institute at Cornell for Nanoscale Science, Cornell University, Ithaca, NY, USA. [5]Canadian Light Source, Saskatoon, Saskatchewan, Canada. [6]Cornell High Energy Synchrotron Source, Cornell University, Ithaca, NY, USA. [7]Leibniz-Institut für Kristallzüchtung, Max-Born-Straße 2, Berlin, Germany. [8]These authors contributed equally: Naman K. Gupta, Rantong Gong, Yi Wu. ✉e-mail: kmshen@cornell.edu; david.hawthorn@uwaterloo.ca

https://doi.org/10.1038/s41467-025-61653-w

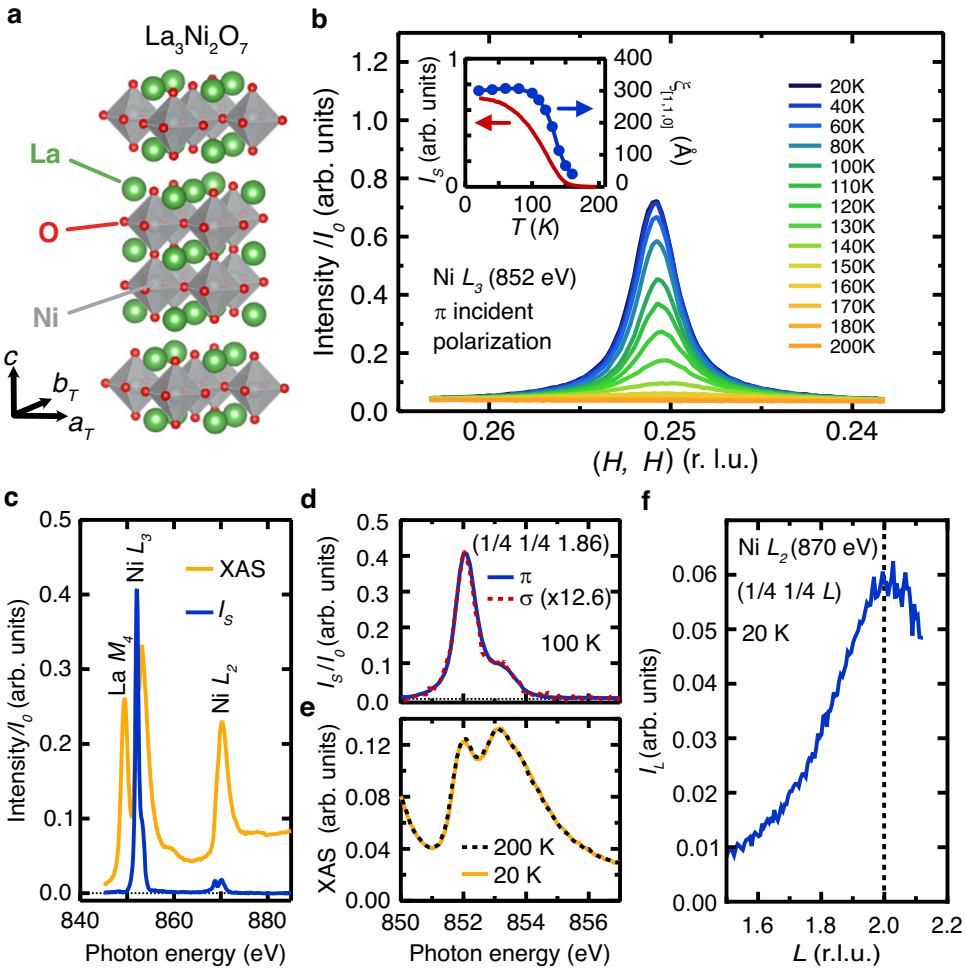

Fig. 1 | Magnetic Resonant Scattering and X-Ray Absorption of $La_3Ni_2O_7$. a The crystal structure of $La_3Ni_2O_7$, with the pseudo tetragonal axes a_T and b_T denoting the in-plane NiO bond directions. **b** The intensity (scattering + background) for cuts along the (H, H, 1.86) direction through the SDW peak at various temperatures, measured at the Ni L_3 absorption edge with π incident polarization for sample A. Inset: The SDW peak amplitude, $I_s(T) = I(T) - I(220K)$ (red), and correlation length along the [1 1 0] direction (blue) as a function of temperature. **c** The energy dependence of the SDW peak amplitude, $I_s(\hbar\omega, 100K) = I(\hbar\omega, 100K) - I(\hbar\omega, 220K)$, measured with π incident light at $L = 1.86$ through the Ni L and La M edges (blue), along with the x-ray absorption (XAS) measured via partial fluorescence yield (orange). The scattering is peaked at the Ni L resonances but is absent off resonance or at the La M_4 resonance. **d** The energy dependence of the SDW peak amplitude at 100 K and $L = 1.86$ at the Ni L_3 edge with σ and π incident light. **e** The Ni L_3 x-ray absorption measured using partial fluorescence yield (PFY) at base temperature (20 K) and above the SDW phase transition (200 K). **f** The L dependence of the SDW structure factor, I_L, at 20 K of the SDW peak at the Ni L_2 edge (870 eV) for sample B.

One of the challenges of investigating $La_3Ni_2O_7$ is the recent discovery of multiple structural polymorphs, including the expected $n = 2$ Ruddlesden-Popper structure comprised of bilayers of NiO_6 octahedra (dubbed 2222), and a surprising naturally-formed superlattice of alternating single-layer and trilayer blocks of NiO_6 octahedra (dubbed 1313)[14,15]. It is plausible that both polymorphs could exist within a single macroscopic bulk crystal sample, and both structures have been reported to be the superconducting phase[15]. Layer-by-layer reactive oxide molecular beam epitaxy (MBE) synthesis of thin films offers a solution to addressing this polymorphism. Here, we focus our investigation on phase-pure epitaxial thin films of the bilayer 2222 polymorph of $La_3Ni_2O_7$. Epitaxial thin films of 16 nm thickness were grown on $NdGaO_3$ (110) substrates using reactive oxide molecular beam epitaxy with shuttered deposition at a pressure of 8×10^{-7} Torr of 80% distilled ozone and a temperature of 800 °C. Samples were characterized by lab-based x-ray diffraction, electrical transport, and synchrotron-based hard x-ray diffraction (see Supplementary Information Section II). 6 samples were synthesized and investigated, and all exhibited qualitatively similar behaviors; data from two samples are shown in this manuscript.

Results

In Fig. 1b, we show RSXS measurements on the Ni L_3 edge in π-polarization along the (H, H, 1.86) direction for a series of temperatures. Here, we employ the pseudo-tetragonal unit cell such at a_T and b_T parallel to the in-plane NiO bond directions. Below 160 K, a sharp peak emerges with $\mathbf{Q}_{SDW}(20\,K) = (0.2508, 0.2508, L)$, slightly incommensurate, but within experimental accuracy of the commensurate value $\left(\frac{1}{4}, \frac{1}{4}, L\right)$. The peak intensity is approximately 45 times stronger in π versus σ polarization at 20 K, suggesting that the scattering originates from magnetic rather than charge ordering, consistent with previous measurements[4]. The resonance energy dependence of the high-temperature background subtracted scattering intensity, $I_s(\hbar\omega, 100K) = I(\hbar\omega, 100K) - I(\hbar\omega, 220\,K)$, at the SDW peak maximum for $L = 1.86$ is shown in Fig. 1c, together with the x-ray absorption spectrum (XAS). This demonstrates that the $\left(\frac{1}{4}, \frac{1}{4}\right)$ Bragg peak is peaked only at the Ni L resonances, and not on the La M_4 edge or off-resonance.

In Fig. 1f, we show the L dependence of the SDW structure factor, I_L, at the in-plane $\left(\frac{1}{4}, \frac{1}{4}\right)$ wavevector on the Ni L_2 edge (870 eV). Note, the L_2 edge is chosen for this purpose for its higher energy and thus a

larger accessible range of L relative to the Ni L_3 edge. While the scattering intensity $I_S(L)$ is peaked at an incommensurate L value (see Supplementary Information Section VI), assessing the L dependence of the SDW structure factor, I_L, requires correction for the variation in the measurement geometry during the L scan to account for both the absorption of the incident and scattered x-rays and the projection photon polarization onto the crystallographic axes. These corrections are akin to the well-known polarization and absorption corrections of conventional x-ray diffraction but are generalized for absorption from a thin film and for resonant scattering from the in-plane magnetic structure identified below (see Supplementary Information Section VI). As shown in Fig. 1f, I_L is peaked at $L = 2$, but with only a 14 ± 4 Å correlation length along the c - direction, revealing the highly two-dimensional nature of the magnetic order in $La_3Ni_2O_7$.

We note that both the resonance energy and L dependence of $\left(\frac{1}{4}, \frac{1}{4}\right)$ SDW Bragg peak establish that the SDW intrinsically originates from $La_3Ni_2O_7$ and not an impurity phase, as has plagued the identification of ostensible charge or spin density order in other related nickelates[16,17]. Specifically, the energy dependence of the scattering is consistent with magnetic order, with a similar energy dependence to other magnetically ordered nickelates[18–20], and is inconsistent with a structural superlattice, such as staged oxygen impurities. The L dependence peaked at an integer L value, indicates the SDW order corresponds to the c-axis lattice constant of $La_3Ni_2O_7$ as opposed to other magnetically ordered compounds such as $RENiO_3$[18–20] or $La_2Ni_2O_5$[21] that also exhibit (1/4, 1/4, L) magnetic order but have different lattice constants and/or order peaked at non-integer values of L.

In many related nickelates in the Ruddlesden-Popper sequence, including $n = 1$ $La_{2-x}Sr_xNiO_4$ and $n = \infty$ perovskite $RENiO_3$ (RE = Nd, Pr, Sm), SDW order coincides with strong charge or bond disproportionation, where the local electronic and orbital environment of the Ni sites is strongly modulated at an atomic scale[18,19,22–27]. Whether such behavior also occurs in $La_3Ni_2O_7$ remains an important open question. Evidence of charge order or bond disproportionation can be most directly identified from the observation of structural changes and superlattice charge peaks. In addition, charge order may exhibit anomalies in transport and thermodynamic properties, such as the metal-insulator transition that is tied to charge disproportionation in $RENiO_3$[24,25], semiconductor-insulator transitions tied to spin-charge order in $La_{2-x}Sr_xNiO_4$[22] or $La_4Ni_3O_8$[28,29], or the metal-metal transition tied to spin-charge order in $La_4Ni_3O_{10}$[30]. In cuprate superconductors, charge order can also be evident in a change in the Hall and Seebeck coefficients, indicative of Fermi surface reconstruction with the onset of CDW order[31].

Evidence of bond disproportionation in $RENiO_3$ is also found in resonant x-ray diffraction and x-ray absorption spectroscopy. In $RENiO_3$, the onset of bond disproportionation leads to spectroscopically distinct Ni sites that can be identified as temperature-dependent changes in the XAS across the metal-insulator transition[32–34]. With resonant x-ray scattering, signatures of bond disproportionation can be detected in the energy and polarization dependence of the resonant scattering. Ni sites having a different orbital occupation and local crystal field, such as long-bond and short-bond Ni sites in $RENiO_3$, will modulate the x-ray scattering form factors on the different Ni sites, leading them to resonate at slightly different energies[35]. These distinct Ni sites also exhibit a different magnitude and orientation of the spin. As the scattering intensity depends on the orientation of the x-ray polarization with respect to the spin, Ni sites with distinct charge environments can result in the linear dichroism of the SDW peak intensity (σ versus π incident polarization) becoming energy dependent (see Supplementary Information Section III), as reported in $RENiO_3$ heterostructures[18].

Considering these signatures of charge order, we find no evidence for charge order or charge disproportionation in our samples of $La_3Ni_2O_7$. We observe no distinct changes in the Ni L edge XAS spectra across T_{SDW} (Fig. 1e), and the linear dichroism of the $\left(\frac{1}{4}, \frac{1}{4}\right)$ peak in $La_3Ni_2O_7$ does not exhibit any observable energy dependence (Fig. 1d), suggesting that all Ni sites have the same orbital occupation and magnitude of spin in the SDW state. In addition, we do not detect strong anomalies in either the resistivity or Hall coefficient (See Supplementary Information Supplementary Fig. S1), nor do we identify evidence of structural phase transitions or superlattice peaks from hard x-ray diffraction (See Supplementary Information section II). While these measurements collectively constitute a null result, they suggest that the dominant order parameter is magnetic and that, unlike many other nickelates, any associated charge modulation in our samples is either absent, does not onset near T_{SDW} or is too weak to be detected in our present measurements.

Measurement of spin configuration

We now determine the orientation of the staggered moments at 20 K, deep within the SDW state. For this, we make use of the sensitivity of the intensity of resonant scattering to the orientation of the photon polarization relative to the magnetic moments, analogous to polarized neutron scattering[18,26,35,36]. The resonant elastic x-ray scattering cross-section is given by refs. 35,37:

$$I^{cr}(\boldsymbol{\epsilon}_{in}, \hbar\omega, \mathbf{Q}) \propto \left| \boldsymbol{\epsilon}^*_{out} \cdot \left(\sum_j F_j(\hbar\omega, \mathbf{Q}) e^{i\mathbf{Q}\cdot\mathbf{r}_j} \right) \cdot \boldsymbol{\epsilon}_{in} \right|^2 \quad (1)$$

where $\hbar\omega$ is the photon energy, $\mathbf{Q} = \mathbf{k}_{out} - \mathbf{k}_{in}$ is the momentum transfer and $\boldsymbol{\epsilon}_{in}$ and $\boldsymbol{\epsilon}_{out}$ are the incident and scattered x-ray polarization, respectively. F_j is a tensor that encodes the photon energy dependence of the scattering cross-section for site j in the lattice, and its elements depend on the orientation of the magnetic moment at site j[35]. (see Supplementary Information section III) Assuming spherical symmetry of the local valence charge density, consistent with the linear dichroism of the SDW peak being energy-independent (Fig. 1d), the scattering depends on the orientation of the staggered $\Delta\mathbf{m}$ as

$$\sum_j F_j(\hbar\omega, \mathbf{Q}) e^{i\mathbf{Q}\cdot\mathbf{r}_j} \propto \begin{bmatrix} 0 & \Delta m_{[001]} & -\Delta m_{[110]} \\ -\Delta m_{[001]} & 0 & \Delta m_{[-110]} \\ \Delta m_{[110]} & -\Delta m_{[-110]} & 0 \end{bmatrix}, \quad (2)$$

where Δm_u are the components of the staggered moments in three orthogonal directions [001], [−110] and [110].

These components can then be deduced by varying the alignment of $\boldsymbol{\epsilon}_{in}$ relative to the [001], [−110] and [110] directions. In an experiment, this is achieved by rotating the sample azimuthally by an angle ϕ about an axis normal to the $\left[\frac{1}{4}, \frac{1}{4}, L\right]$ set of lattice planes (here L is 1.93), as depicted in Fig. 2a, which is accomplished by mounting the c-axis normal film on a 43.7° wedge. This approach enables the orientation of the moments to be rotated relative to the incident polarization, which can be set to be π, σ, circular or linear 45° ($\pi - \sigma$), with the scattering wavevector remaining centered on the $(1/4, 1/4, 1.93)$ peak. As shown in Fig. 2b, the scattering intensity, measured here at 20 K, has a strong dependence on the azimuthal angle, ϕ as well as on the polarization of the incident light. In Fig. 2c, we plot the SDW peak amplitude as a function of azimuthal angle ϕ, for our various incident polarizations. Notably, the peak intensity exhibits a complex, non-monotonic dependence with ϕ and large variations with incident polarization. This azimuthal dependence can be compared to simulations of the staggered moments oriented along different directions, calculated using Eqs. 1 and 2, the sample geometry, and a correction for the geometry-dependent absorption of the incident and scattered x-rays (Supplementary Information Section IIIB). As shown in Fig. 2c the measurements show remarkable agreement with the moments forming diagonal, bicollinear spin stripes (Fig. 2d) with the magnetic

https://doi.org/10.1038/s41467-025-61653-w

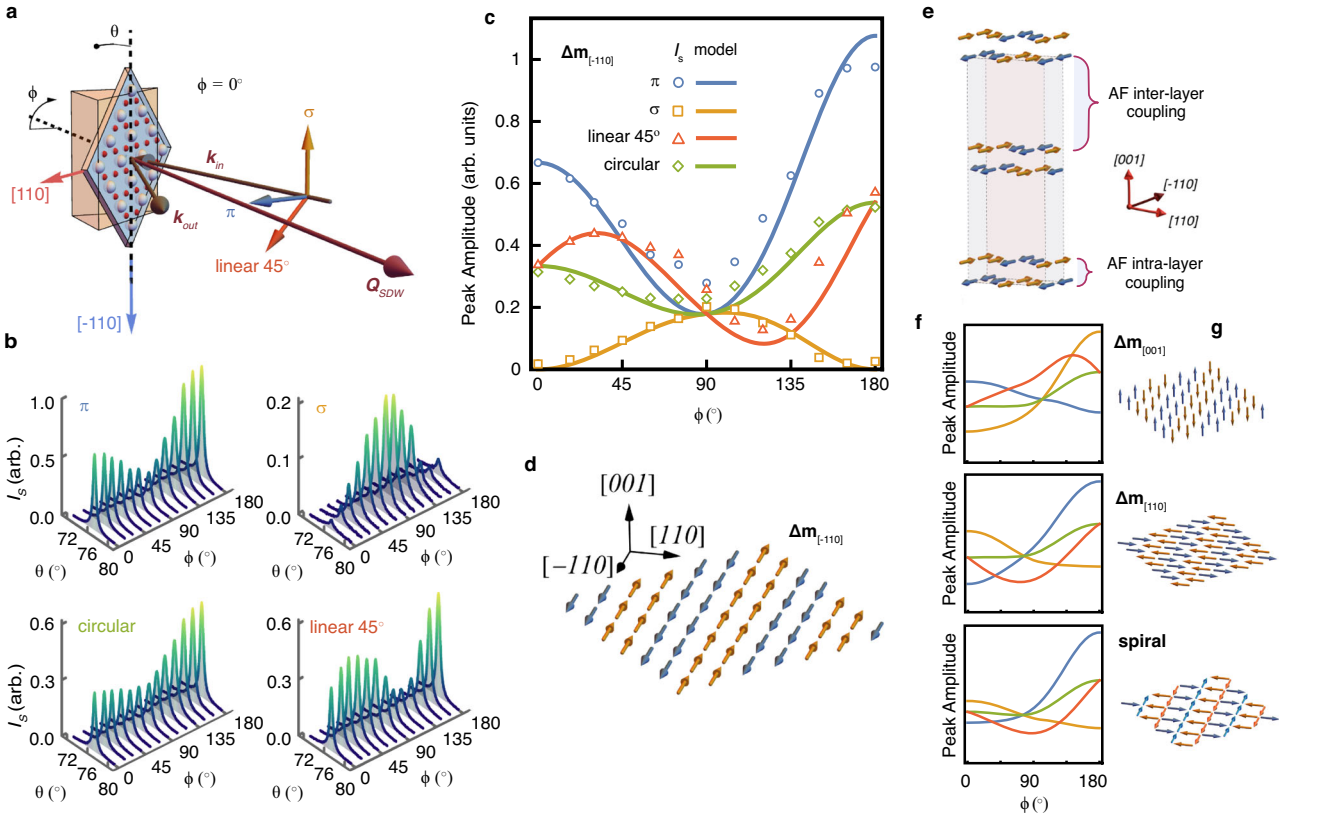

Fig. 2 | Measuring Orientation of Magnetic Moments. a The measurement geometry for azimuthal angle (ϕ) dependent measurements. The sample is mounted on a 43.7 deg wedge to align the $\left[\frac{1}{4},\frac{1}{4},1.93\right]$ set of planes with the azimuthal rotation axis. The incident photon polarization is set to be σ, π, linear 45° (π − σ) or circular. The sample was rocked about the vertical axis by angle θ to measure the intensity and width of the $\left(\frac{1}{4},\frac{1}{4},1.93\right)$ SDW peak. **b** The scattering intensity, $I_s = I(T) - I(200K)$, versus θ through the SDW peak at ϕ values between 0 and 180 degrees for π, σ, circular and linear 45° incident x-ray polarization at 20 K. The scattering intensity, I_S, is found by subtracting the background fluorescence measured above T_{SDW} (200 K) from the total intensity (scattering + background fluorescence) measured at 20 K. **c** The SDW peak amplitude, I_S, at 20 K versus ϕ for π, σ, circular and linear 45° incident polarization. Solid lines are the ϕ dependence calculated for a magnetic structure with **Δm** parallel to [−110], depicted in (**d**). **e** The 3D magnetic unit cell is deduced from the azimuthal angle dependence and assuming anti-ferromagnetic bilayer coupling. **f** The ϕ and polarization dependence that would result from the spin configurations depicted in (**g**).

moments lying entirely within the $a-b$ plane but oriented perpendicular to $\mathbf{Q}_{SDW}$. We emphasize this model was calculated without any free-fitting parameters, apart from an overall scaling factor.

In contrast, the calculated polarization and ϕ dependence for other possible SDW scenarios (Fig. 2f, g), including **Δm** out of the plane, **Δm** ∥ $\mathbf{Q}_{SDW}$, or a non-collinear configuration, all bear no qualitative resemblance to the experimental data (Fig. 2c), indicating the relative contribution of **Δm** out of the NiO plane or parallel to $\mathbf{Q}_{SDW}$ is less than a few percent at 20 K.

Having constrained the orientation of moments predominantly within the NiO_2 planes, we can now consider the full 3D magnetic structure, which is informed by the L dependence of the SDW scattering cross-section. The fact that the SDW order is peaked at $L = 2$ and is minimal at $L = 1.5$, (Fig. 1f) indicates that with the coupling within the bilayer (intra-bilayer coupling) and between bilayers (inter-bilayer coupling) are either both ferromagnetic or both antiferromagnetic (see Supplemental Information Section VI). Given that the reasonably straight interlayer Ni-O-Ni bond is likely to involve antiferromagnetic super-exchange and that the experimental magnon dispersion is well described by a model with a large AF bilayer coupling[2], this suggests the magnetic structure is consistent with the one depicted in Fig. 2e, with both inter- and intra-bilayer AF coupling.

This bicollinear double spin-stripe configuration is notably different from many other nickelates, including the non-collinear spin-spiral magnetic order in thin films of $RENiO_3$[18–20], the collinear order with moments parallel to $\left(\frac{1}{4},\frac{1}{4},\frac{1}{4}\right)$ in ultrathin $RENiO_3$[18], spin/charge stripes with moments perpendicular to the planes in the square-planar trilayer nickelate $La_4Ni_3O_8$[29], the reported magnetic order, with moments along c, in $La_2Ni_2O_5$[23], and spin-stripe order in $La_{2-x}Sr_xNiO_4$[38,39], which has staggered moments oriented within the NiO planes but not perpendicular to $\mathbf{Q}_{SDW}$. Staggered moments in the NiO planes and perpendicular to $\mathbf{Q}_{SDW}$ are found in both single-layer $La_2NiO_{4+\delta}$ [27] and the trilayer $La_4Ni_3O_{10}$[30,40], suggesting a potential link between the SDW in these compounds and $La_3Ni_2O_7$. However, these compounds both exhibit spin-charge stripe order, with $La_2NiO_{4+\delta}$ being an insulator and $La_4Ni_3O_{10}$ having incommensurate spin-charge stripe order. In both wavevector and orientation of moments, the SDW order in $La_3Ni_2O_7$ is also similar to the bicollinear double spin stripe observed in FeTe[41–43].

Anisotropic, unidirectional magnetic domains

The unidirectional, stripe-like character of the antiferromagnetic order is also manifest in the shape of the SDW domains, which break the rotational symmetry of the lattice. We measured the shapes and intensities of the SDW Bragg peaks in the $H-K$ plane for both sets of SDW domains with orthogonal **Q** vectors, around $\left(\frac{1}{4},\frac{1}{4},L\right)$ (in red) and $\left(\frac{1}{4},-\frac{1}{4},L\right)$ (in blue) using a two-dimensional microchannel plate detector, shown in Fig. 3a. The Bragg peaks around $\left(\frac{1}{4},\frac{1}{4},L\right)$ and $\left(\frac{1}{4},-\frac{1}{4},L\right)$ have equal intensities to within experimental uncertainty (±3 %), indicating an equal population of domains. In both sets of domains, the SDW peaks have highly anisotropic shapes, with a 2D

https://doi.org/10.1038/s41467-025-61653-w

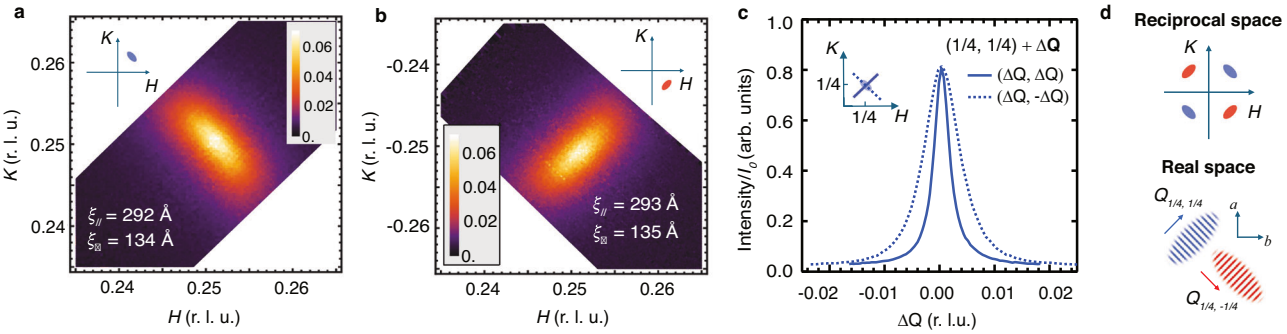

Fig. 3 | Anisotropic Bragg peaks indicative of stripe-like SDW domains. The shape of the (**a**) (1/4 1/4 *L*) and (**b**) (1/4 -1/4 *L*) Bragg peaks at 852 eV with π incident polarization. Measurement of *H* and *K* for sample A using a 2D channelplate detector (integrated between *L* = 1.81 and 1.90). The orthogonal peaks have the same intensities and widths. **c** Cuts through the (1/4 1/4 1.85) Bragg peak parallel and perpendicular to the in-plane **Q** vector. **d** The shape of Bragg peaks in reciprocal space and the corresponding domain structure in real space for anisotropic domains of unidirectional stripe order, consistent with the measurements in (**a**) and (**b**).

Lorentzian fit giving correlation lengths that are much longer parallel to $\mathbf{Q}_{SDW}$ ($\xi_{\parallel} = 292$ Å) versus perpendicular to $\mathbf{Q}_{SDW}$ ($\xi_{\perp} = 134$ Å).

This peak shape is consistent with anisotropic domains of unidirectional SDW order, with each domain characterized by either (1/4, 1/4) or (-1/4, 1/4) order, as depicted in Fig. 3d. This anisotropy could be associated with orthorhombic structural twin domains or maybe orthogonal domains of unidirectional order occurring within a single structural domain. Intriguingly, this latter scenario is reminiscent of the anisotropic charge ordering reported in underdoped $YBa_2Cu_3O_{7-\delta}$ and $Bi_2Sr_{2-x}La_xCuO_{6+\delta}$, where the CDW Bragg peaks likewise exhibit an anisotropy, with longer correlations lengths parallel to the CDW wavevector, indicative of orthogonal anisotropic unidirectional CDW domains within a single orthorhombic structural domain[44,45].

Probing magnetic domain walls

In Fig. 2, the orientation of the staggered moment at 20 K was determined to be almost entirely within the $a-b$ plane and perpendicular to $\mathbf{Q}_{SDW}$ (i.e., $\Delta\mathbf{m} \parallel [-1, 1, 0]$ for $\mathbf{Q}_{SDW} = (1/4, 1/4, L)$ domains or $\Delta\mathbf{m} \parallel [1, 1, 0]$ for $\mathbf{Q}_{SDW} = (-1/4, 1/4, L)$ domains). Insights may be gleaned from the small discrepancies between the model and measurements. In particular, measurements using σ polarization at $\phi = 0$ are at a minimum in intensity for this magnetic orientation, with deviations of the staggered moment in the NiO planes, but parallel to $\mathbf{Q}_{SDW}$ and/or along [001] required to provide a finite scattering intensity. We now leverage this sensitivity of the polarization to the staggered moment orientation to investigate how the spin configuration evolves with temperature. In Fig. 4b, we show a comparison between the temperature dependence of the SDW peak when measured with π versus σ polarization. At low temperatures ($T < 50\,K$), the scattering intensity of the SDW peak measured in π polarization, I_π, is more than an order of magnitude stronger than in σ polarization, I_σ. Upon raising the temperature to T_{SDW}, I_π, smoothly decreases whereas I_σ exhibits a non-monotonic temperature dependence, growing in intensity before peaking around 130 K, and then falling rapidly to zero at T_{SDW}. On the other hand, the ratio of I_σ / I_π, shown in Fig. 4c grows smoothly and monotonically with increasing temperature all the way up to T_{SDW} when the peak vanishes, indicating that the component of the spins oriented away from the low T configuration (Fig. 2c) grows with increasing temperature, with $I_\sigma/I_\pi > 0.6$ near T_{SDW}.

In addition to this anomalous temperature dependence, the width of the SDW Bragg peak is surprisingly broader when measured with σ versus π incident polarization (Fig. 4a, d) Note, in Fig. 4d the peak width with σ polarization is deduced by subtracting a narrow peak resulting from ~ 1.5% π incident light in the nominally σ polarized beam, as discussed in Supplementary Information Section VII. The broader peak with σ incident polarization indicates that the staggered moments parallel to $\mathbf{Q}_{SDW}$ or along [001] (probed with σ incident light) have a shorter correlation length at low temperatures than the predominant spin configuration with staggered moments in the NiO plane and perpendicular to $\mathbf{Q}_{SDW}$. This observation would be inconsistent with a uniform, temperature-dependent canting of all the spins. Instead, this could be consistent with the existence of real-space defects of the magnetic order, such as Bloch-like domain walls or antiferromagnetic skyrmion-like topological defects. Indeed, Bloch-like domain walls may naturally exist between two orthogonal unidirectional domains, where the transition between domains would necessitate a reorientation of the spins by 90° from one domain to its orthogonal counterpart, which could occur over an extended region, depending on the relative magnitude of the magnetic anisotropy and exchange terms.

In our interpretation of the data in terms of Bloch domain walls, the staggered moments would rotate away from [110] or [−110] and out of the $a-b$ plane, as depicted conceptually in Fig. 5. Here, I_π would probe the bicollinear spin stripe regions within the core of each domain, while I_σ would be sensitive to the rotated spin component in the domain walls. The relative volume fraction of domain walls would grow with increasing temperature until SDW order is lost at T_{SDW}. This interpretation could explain the broader peak for I_σ when compared to I_π, as shown in Fig. 4d. Finally, the influence of the domain walls may also be the source of the small deviations from a perfectly in-plane moment at 20 K depicted in Fig. 2c. This analysis represents a possible new approach to detecting defects in antiferromagnetic order. Unlike ferromagnetic domain walls, antiferromagnetic domain walls are often difficult to detect[46]. Further analysis of the polarization and temperature dependence of the (1/4 1/4) SDW peaks in $La_3Ni_2O_7$ may provide key insights into the width, density and detailed magnetic configuration of the domain walls. Such investigations may be of key importance as the magnetic configuration close to T_{SDW}, including a high density of domain walls, may represent the melting of long-range SDW order as the material approaches its superconducting phase.

Discussion

A comparison between these experiments with those on bulk crystals[4] reveal a number of commonalities, including similar T_{SDW}'s, temperature dependences, photon polarization dependence, and peak widths along the (H H L) direction, suggesting that the results reported here are universal to both bulk and thin film samples.

The structure of the bicollinear spin stripe order in $La_3Ni_2O_7$ bears a strong resemblance to the magnetically ordered state in FeTe, but with a major distinction: in FeTe, the spin stripe ordering is accompanied by a monoclinic structural transition that stabilizes the magnetic order[43,47,48]. In contrast, temperature-dependent, synchrotron-

https://doi.org/10.1038/s41467-025-61653-w

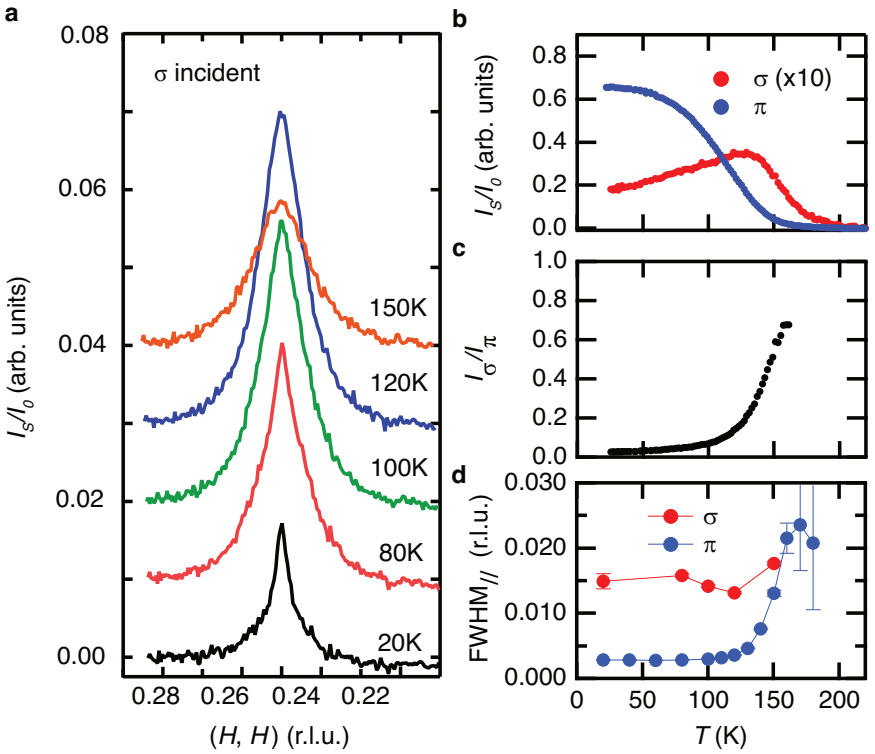

Fig. 4 | Temperature dependence of (1/4 1/4 *L*) Bragg peak with σ photon polarization. a Cuts of the scattering intensity through the SDW peak at $L = 1.93$ and 852 eV with incident σ photon polarization at various temperatures. The peak is broader with σ polarization than with π polarization (Fig. 1b) and exhibits a non-monotonic temperature dependence. **b** The temperature dependence of the (1/4 1/4 1.93) peak amplitude, I_s, with σ and π incident polarization. The peak emerges at 200 K, but peaks at 130 K with σ polarization. **c** The ratio of the scattering intensity from σ and π incident light, I_σ/I_π, which increases monotonically with increasing temperature. **d** The FWHM of the (1/4 1/4) peak with σ and π incident light. As described in supplementary section VII, I_S with σ incident light is fit to two peaks (broad and narrow). The narrow peak has FWHM comparable to the I_S with π incident light and is evident at 20 K in **a**) but diminished above 100 K. We attribute the narrow peak to an artifact of a few percent contribution of π incident light in the nominal σ polarized beam. The FWHM of the remaining broad peak is shown in d).

based hard x-ray diffraction measurements of our $La_3Ni_2O_7$ thin films do not reveal any lowering of structural symmetry or the appearance of superlattice peaks upon entering the SDW state (see Supplementary Information Section II). Furthermore, the existence of domain walls or topological defects indicates that both orthogonal magnetic domains occur within a single NiO_2 plane. This may imply an inherent instability in $La_3Ni_2O_7$ to rotational symmetry breaking, possibly accompanied by disordered or frustrated nematic order[11], analogous to the Fe-based and cuprate superconductors where unidirectional density wave and nematic orders are pervasive and closely intertwined with superconductivity[12,13]. These analogies with the cuprates and Fe-based superconductors suggest that the fluctuation of this SDW state is related to the formation of the superconducting state under high pressure.

Methods

Two samples A and B were measured for this study. A more extensive set of data was measured for sample A. However, sample B was found to have comparable peak intensity, peak width, and temperature dependence as sample A, as well as reproducing the anisotropy in the width parallel and perpendicular to $\boldsymbol{Q}$ (see Supplementary Information section V).

Resonant soft x-ray scattering measurements were performed at the Canadian Light Source REIXS beamline[49]. The majority of the measurements were made using an energy-resolved silicon drift detector, with measurements of the peak shape utilizing a 2D micro-channel plate detector. The silicon drift detector the detector resolution corresponds to $\Delta H = 0.00124$ reciprocal lattice units, compared to a peak width of 0.0028 FWHM for π incident polarization at 20 K (Fig. 4d). This leads to an increase in the peak width due to measurement resolution of ~10% at base temperature with π incident polarization. The pixel size of the 2D micro-channel plate detector used for Fig. 3a, b is $\Delta H = 0.00006$ reciprocal lattice units, far below the measured peak widths.

The samples were oriented using the (110) Bragg peak of the $NdGaO_3$ (NGO) substrate at 2500 eV. The in-plane orientation was performed using $(\frac{1}{4}, \frac{1}{4}, L)$ SDW Bragg peaks at 852 eV. The samples were found to have a *c*-axis lattice constant of 20.44 Å from lab-based x-ray diffraction. Reciprocal space maps show lattice matching to the NGO substrate, which for the [110] surface of NGO imparts in-plane lattice constants of $a_T = 3.844$ Å and $b_T = 3.858$ Å at 100 K[50]. The mosaic spread of La327 films was measured to be less than 0.007° FWHM, much smaller than the angular width of the SDW peaks.

The scattering intensities, I_S, shown in Figs. 1b (inset), c, d, 2b, 3c and 4, are deduced by subtracting the background intensity measured above the SDW transition (at 200 K or 220 K) from the measured intensity at lower temperature.

The correlation length, ξ_u, along different directions u, was determined from Lorentzian fits to the data of the form given in eq. 3 (or using an equivalent expression in reduced co-ordinates *H* and *K*):

$$\frac{Amplitude}{\left(\frac{(\mathbf{Q}-\mathbf{Q}_{SDW})\cdot\frac{1}{\sqrt{2}}(1,1,0)}{\frac{\Gamma_{[110]}}{2}}\right)^2+\left(\frac{(\mathbf{Q}-\mathbf{Q}_{SDW})\cdot\frac{1}{\sqrt{2}}(1,-1,0)}{\frac{\Gamma_{[1-10]}}{2}}\right)^2+1} \quad (3)$$

where $\mathbf{Q} = (\frac{2\pi}{a_T} H, \frac{2\pi}{a_T} K)$, $\mathbf{Q}_{SDW}$ is the in-plane wavevector of the SDW peak maximum, and Γ_u is an inverse correlation length. The correlation length is given by $\xi_u = 2/\Gamma_u$.

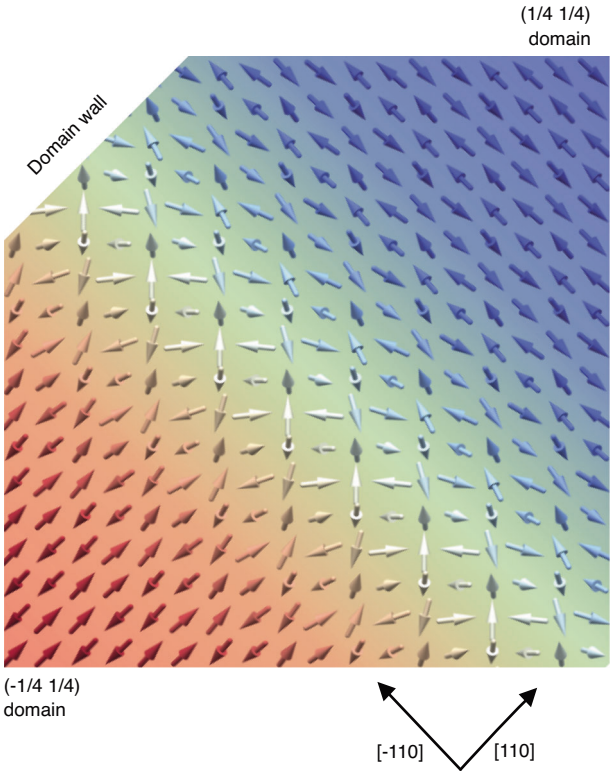

Fig. 5 | Conceptual representation of a magnetic domain wall between $Q_{(110)}$ and between $Q_{(-110)}$ SDW domains. In the vicinity of a domain wall, the spin orientation may rotate to have a sizeable, staggered moment out of the plane and/or parallel to $\boldsymbol{Q}$.

For measurements with σ incident polarization, shown in Fig. 4, the incident beam includes a small ($\simeq$1.5%) π contribution due to synchrotron light from bending chicane magnets that is in addition to the primary σ polarized light from the EPU. In 4 d, the full width at half maximum (FWHM) with σ polarization is determined by fitting the data in Fig. 4a to a narrow peak from π polarized light, with FWHM equal to that of a pure π polarization (blue curve in Fig. 4d), as well as broader peak with σ polarization (red curve in Fig. 4d).

Figure 1a with the crystal structure of $La_3Ni_2O_7$ was generated using VESTA[51].

Reporting summary

Further information on research design is available in the Nature Portfolio Reporting Summary linked to this article.

Data availability

All data needed to evaluate the conclusions in the paper are present in the manuscript and supplementary information. Correspondence and requests for materials should be addressed to K.M. Shen (kmshen@cornell.edu) and D.G. Hawthorn (david.hawthorn@uwaterloo.ca).

References

1. Sun, H. et al. Signatures of superconductivity near 80 K in a nickelate under high pressure. *Nature* **621**, 493–498 (2023).
2. Keimer, B., Kivelson, S. A., Norman, M. R., Uchida, S. & Zaanen, J. From quantum matter to high-temperature superconductivity in copper oxides. *Nature* **518**, 179 (2015).
3. Fernandes, R. M. et al. Iron pnictides and chalcogenides: a new paradigm for superconductivity. *Nature* **601**, 35 (2022).
4. Chen, X. et al. Electronic and magnetic excitations in $La_3Ni_2O_7$. *Nat. Commun.* **15**, 9597 (2024).
5. Liu, Z. et al. Evidence for charge and spin density waves in single crystals of $La_3Ni_2O_7$ and $La_3Ni_2O_6$. *Sci. China Phys. Mech. Astron* **66**, 217411 (2022).
6. Wu, G., Neumeier, J. J. & Hundley, M. F. Magnetic susceptibility, heat capacity, and pressure dependence of the electrical resistivity of $La_3Ni_2O_7$ and $La_4Ni_3O_{10}$. *Phys. Rev. B* **63**, 245120 (2001).
7. Kakoi, M. et al. Multiband metallic ground state in multilayered nickelates $La_3Ni_2O_7$ and $La_4Ni_3O_{10}$ probed by ^{139}La-NMR at ambient pressure. *J. Phys. Soc. Jpn.* **93**, 053702 (2024).
8. Dan, Z. et al. Pressure-enhanced spin-density-wave transition in double-layer nickelate $La_3Ni_2O_7$. *Sci. Bull.***70**, 1239–1245 (2025).
9. Chen, K. et al. Evidence of spin density waves in $La_3Ni_2O_{7-\delta}$. *Phys. Rev. Lett.* **132**, 256503 (2024).
10. Khasanov, R. et al. Pressure-induced splitting of density wave transitions in $La_3Ni_2O_{7-\delta}$. *Nat. Phys.* **21**, 430–436 (2025).
11. Böhmer, A. E., Chu, J.-H., Lederer, S. & Yi, M. Nematicity and nematic fluctuations in iron-based superconductors. *Nat. Phys.* **18**, 1412–1419 (2022).
12. Fradkin, E., Kivelson, S. A. & Tranquada, J. M. Colloquium: Theory of intertwined orders in high temperature superconductors. *Rev. Mod. Phys.* **87**, 457–482 (2015).
13. Fernandes, R. M., Orth, P. P. & Schmalian, J. Intertwined vestigial order in quantum materials: Nematicity and beyond. *Annu. Rev. Condens. Matter Phys.* **10**, 133–154 (2019).
14. Chen, X. et al. Polymorphism in Ruddlesden-Popper $La_3Ni_2O_7$: Discovery of a hidden phase with distinctive layer stacking. *J. Am. Chem. Soc.* **146**, 3640–3645 (2024).
15. Puphal, P. et al. Unconventional crystal structure of the high-pressure superconductor $La_3Ni_2O_7$. *Phys. Rev. Lett.* **133**, 146002 (2024).
16. Parzyck, C. T. et al. Absence of $3a_0$ charge density wave order in the infinite-layer nickelate $NdNiO_2$. *Nat. Mater.* **23**, 486–491 (2024).
17. Wang, B.-X. et al. Antiferromagnetic defect structure in $LaNiO_{3-\delta}$ single crystals. *Phys. Rev. Mater.* **2**, 064404 (2018).
18. Hepting, M. et al. Complex magnetic order in nickelate slabs. *Nat. Phys.* **14**, 1097–1102 (2018).
19. Scagnoli, V. et al. Role of magnetic and orbital ordering at the metal insulator transition in $NdNiO_3$. *Phys. Rev. B* **73**, 100409 (2006).
20. Frano, A. et al. Orbital control of noncollinear magnetic order in nickel oxide heterostructures. *Phys. Rev. Lett.* **111**, 106804 (2013).
21. Alonso, J. A., Martínez-Lope, M. J., García-Muñoz, J. L. & Fernández-Díaz, M. T. A structural and magnetic study of the defect perovskite from high-resolution neutron diffraction data. *J. Phys. Condens. Matter* **9**, 6417 (1997).
22. García-Muñoz, J. L., Rodríguez-Carvajal, J. & Lacorre, P. Neutron-diffraction study of the magnetic ordering in the insulating regime of the perovskites $RNiO_3$ (R=Pr and Nd). *Phys. Rev. B* **50**, 978 (1994).
23. Imada, M., Fujimori, A. & Tokura, Y. Metal-insulator transitions. *Rev. Mod. Phys.* **70**, 1039 (1998).
24. Hepting, M. et al. Tunable charge and spin order in $PrNiO_3$ thin films and superlattices. *Phys. Rev. Lett.* **113**, 227206 (2014).
25. Alonso, J. A. et al. Charge disproportionation in $RNiO_3$ perovskites: Simultaneous metal-insulator and structural transition in $YNiO_3$. *Phys. Rev. Lett.* **82**, 3871 (1999).
26. Scagnoli, V. et al. Induced noncollinear magnetic order of Nd^{3+} in $NdNiO_3$ observed by resonant soft x-ray diffraction. *Phys. Rev. B* **77**, 115138 (2008).
27. Tranquada, J. M., Lorenzo, J. E., Buttrey, D. J. & Sachan, V. Cooperative ordering of holes and spins in $La_2NiO_{4.125}$. *Phys. Rev. B* **52**, 3581 (1995).
28. Zhang, J. et al. Stacked charge stripes in the quasi-2D trilayer nickelate $La_4Ni_3O_8$. *Proc. Natl. Acad. Sci. USA* **113**, 8945 (2016). URL.
29. Zhang, J. et al. Spin stripe order in a square planar trilayer nickelate. *Phys. Rev. Lett.* **122**, 247201 (2019).

30. Zhang, J. et al. Intertwined density waves in a metallic nickelate. *Nat. Commun.* **11**, 6003 (2020).
31. Taillefer, L. Fermi surface reconstruction in high-*Tc* superconductors. *J. Phys. Condens. Matter* **21**, 164212 (2009).
32. Piamonteze, C. et al. Spin-orbit-induced mixed-spin ground state in $RNiO_3$ perovskites probed by x-ray absorption spectroscopy: Insight into the metal-to-insulator transition. *Phys. Rev. B* **71**, 020406 (2005).
33. Liu, J. et al. Strain-mediated metal-insulator transition in epitaxial ultra thin films of $NdNiO_3$. *Appl. Phys. Lett.* **96**, 233110 (2010).
34. Bruno, F. Y. et al. Probing the metal-insulator transition in nickelates using soft x ray absorption spectroscopy. *Appl. Phys. Lett.* **104**, 021920 (2014).
35. Haverkort, M. W., Hollmann, N., Krug, I. P. & Tanaka, A. Symmetry analysis of magneto-optical effects: The case of x-ray diffraction and x-ray absorption at the transition metal $L_{2,3}$ edge. *Phys. Rev. B* **82**, 094403 (2010).
36. Hannon, J. P., Trammell, G. T., Blume, M. & Gibbs, D. X-ray resonance exchange scattering. *Phys. Rev. Lett.* **61**, 1245–1248 (1988).
37. Fink, J., Schierle, E., Weschke, E. & Geck, J. Resonant elastic soft x-ray scattering. *Rep. Prog. Phys.* **76**, 056502 (2013).
38. Lee, S.-H., Cheong, S.-W., Yamada, K. & Majkrzak, C. F. Charge and canted spin order in $La_{2-x}Sr_xNiO_4$ (x=0.275 and 1/3). *Phys. Rev. B* **63**, 060405 (2001).
39. Merritt, A. M., Reznik, D., Garlea, V. O., Gu, G. D. & Tranquada, J. M. Nature and impact of stripe freezing in $La_{1.67}Sr_{0.33}NiO_4$. *Phys. Rev. B* **100**, 195122 (2019).
40. Samarakoon, A. M. et al. Bootstrapped dimensional crossover of a spin density wave. *Phys. Rev. X* **13**, 041018 (2023).
41. Dai, P. Antiferromagnetic order and spin dynamics in iron-based superconductors. *Rev. Mod. Phys.* **87**, 855–896 (2015).
42. Rodriguez, E. E. et al. Magnetic-crystallographic phase diagram of the superconducting parent compound $Fe_{1+x}Te$. *Phys. Rev. B* **84**, 064403 (2011).
43. Li, S. et al. First-order magnetic and structural phase transitions in $Fe_{1+y}Se_xTe_{1-x}$. *Phys. Rev. B* **79**, 054503 (2009).
44. Comin, R. et al. Broken translational and rotational symmetry via charge stripe order in underdoped $YBa_2Cu_3O_{6+y}$. *Science* **347**, 1335–1339 (2015).
45. Choi, J. et al. Universal stripe symmetry of short-range charge density waves in cuprate superconductors. *Adv. Mater.* **36**, 2307515 (2024).
46. Cheong, S.-W., Fiebig, M., Wu, W., Chapon, L. & Kiryukhin, V. Seeing is believing: visualization of antiferromagnetic domains. *NPJ Quantum Mater.* **5**, 1–10 (2020).
47. Bao, W. et al. Tunable ($\delta\pi$, $\delta\pi$)-type antiferromagnetic order in α Fe(Te,Se) superconductors. *Phys. Rev. Lett.* **102**, 247001 (2009).
48. Rodriguez, E. E. et al. Magnetic and structural properties near the lifshitz point in $Fe_{1+x}Te$. *Phys. Rev. B* **88**, 165110 (2013).
49. Hawthorn, D. G. et al. An in-vacuum diffractometer for resonant elastic soft x-ray scattering. *Rev. Sci. Instrum.* **82**, 073104 (2011).
50. Vasylechko, L. et al. The crystal structure of $NdGaO_3$ at 100 K and 293 K based on synchrotron data. *J. Alloy. Compd.* **297**, 46 (2000).
51. Momma, K. & Izumi, F. VESTA 3 for three-dimensional visualization of crystal, volumetric and morphology data. *J. Appl. Crystallogr.* **44**, 1272–1276 (2011).

Acknowledgements

This work was primarily supported by the National Science Foundation through Grant No. DMR-2104427 (K.M.S.), the Air Force Office of Scientific Research (Grant No. FA955021–1-0168, FA9550-23–1-0161; K.M.S.) and the Natural Sciences and Engineering Research Council (NSERC) of Canada (D.G.H.). The Platform for the Accelerated Realization, Analysis and Discovery of Interface Materials (PARADIM) under Cooperative Agreement No. DMR-2039380 supported optimization of film growth parameters and structural characterization (D.G.S. and K.M.S.). The U.S. Department of Energy, Office of Basic Energy Sciences under contract no. DE-SC0019414 (B.Z.G, A.S., D.G.S., K.M.S.) supported the hard x-ray synchrotron diffraction work at CHEXS. Additional support for materials synthesis was provided by the Gordon and Betty Moore Foundation's EPiQS Initiative through Grant Nos. GBMF3850 and GBMF9073 (D.G.S.). N.K.G. acknowledges support from the Waterloo Institute of Nanotechnology (WIN). This work is based on research conducted at the Center for High-Energy X-ray Sciences (CHEXS), which is supported by the National Science Foundation (BIO, ENG and MPS Directorates) under award DMR-1829070. Part of the research described in this paper was performed at the Canadian Light Source, a national research facility of the University of Saskatchewan, which is supported by the Canada Foundation for Innovation (CFI), the Natural Sciences and Engineering Research Council (NSERC), the National Research Council Canada (NRC), the Canadian Institutes of Health Research (CIHR), the Government of Saskatchewan, and the University of Saskatchewan. Substrate preparation was performed in part at the Cornell NanoScale Facility, a member of the National Nanotechnology Coordinated Infrastructure, which is supported by the NSF (Grant No. NNCI-2025233); the authors would like to thank Sean Palmer and Steven Button for their assistance in substrate preparation and Michel Gingras for discussions.

Author contributions

D.G.H. and K.M.S. conceived of, designed, and supervised the experiment. N.K.G. conceived the experiment and identified anisotropy in the SDW peak shape. The resonant scattering experiments were performed by N.K.G., R.G., M.K., C.T.P., N.C., R.S., and D.G.H. Samples were synthesized and characterized by Y.W. with assistance from C.T.P., D.G.S., and K.M.S. Hard X-ray scattering measurements were conducted and analyzed by B.Z.G., S.S. and A.S. The data were analyzed by N.K.G., R.G., C.T.P., K.M.S. and D.G.H. Model calculations were performed by D.G.H. The manuscript was written by D.G.H. and K.M.S. with input from all authors.

Competing interests

The authors declare no competing interests.

Additional information

Supplementary information The online version contains supplementary material available at https://doi.org/10.1038/s41467-025-61653-w.

Correspondence and requests for materials should be addressed to Kyle M. Shen or David G. Hawthorn.

Peer review information *Nature Communications* thanks the anonymous reviewers for their contribution to the peer review of this work. A peer review file is available.

Supplementary Information for: Anisotropic Spin Stripe Domains in Bilayer $La_3Ni_2O_7$

N. K. Gupta,[1] R. Gong,[1] Y. Wu,[2] M. Kang,[2,3,4] C. T. Parzyck,[2] B. Z. Gregory,[2,3] N. Costa,[1]
R. Sutarto,[5] S. Sarker,[6] A. Singer,[3] D. G. Schlom,[3,4,7] K. M. Shen,[2,4,*] and D. G. Hawthorn[1,*]

[1]*Department of Physics and Astronomy, University of Waterloo, Waterloo ON N2L 3G1, Canada*
[2]*Laboratory of Atomic and Solid State Physics, Department of Physics, Cornell University, Ithaca, NY 14853, USA*
[3]*Department of Materials Science and Engineering, Cornell University, Ithaca, NY 14853, USA*
[4]*Kavli Institute at Cornell for Nanoscale Science, Cornell University, Ithaca, NY 14853, USA*
[5]*Canadian Light Source, Saskatoon SK S7N 2V3, Canada*
[6]*Cornell High Energy Synchrotron Source, Cornell University, Ithaca, NY 14853, USA*
[7]*Leibniz-Institut für Kristallzüchtung, Max-Born-Straße 2, 12489 Berlin, Germany*

I. SAMPLE SYNTHESIS AND CHARACTERIZATION

Bilayer $La_3Ni_2O_7$ films were grown on $NdGaO_3$(110) substrates using reactive-oxide molecular-beam epitaxy in a Veeco GEN10 system using elemental sources of La (Alfa Aesar, 99.900%) and Ni (Alfa Aesar, 99.995%). The substrates were annealed before growth at 750° C until a clear reflection high-energy electron diffraction (RHEED) pattern was observed. Growths were performed at substrate thermocouple temperatures between 790 and 750° C (pyrometer temperature of 630° C) in background pressures between 7 and 8 $\times 10^{-7}$ torr of 80 % distilled ozone. Initial flux calibration was performed by monitoring RHEED oscillations during the growths of binary oxides La_2O_3 on $(ZrO_2)_{0.905}(Y_2O_3)_{0.095}$ (111) and NiO on MgO (100). Further stoichiometric and flux optimization was achieved by minimizing the $LaNiO_3$ $(002)_{pc}$ plane spacing and optimizing the residual resistivity ratio (RRR) of the $LaNiO_3$ film.

The structural quality of both perovskite and high-order Ruddlesden-Popper (RP) phase samples was determined using Cu $K\alpha_1$ X-ray diffraction (XRD) measurements performed on a PANalytical Empyrean X-ray diffractometer, shown in figure S1 a). Resistivity and Hall effect measurements (figure S1 b) and c) were conducted using a Quantum Design Physical Property Measurement System down to 2 K. Contacts were prepared by ultrasonic aluminum wire bonding.

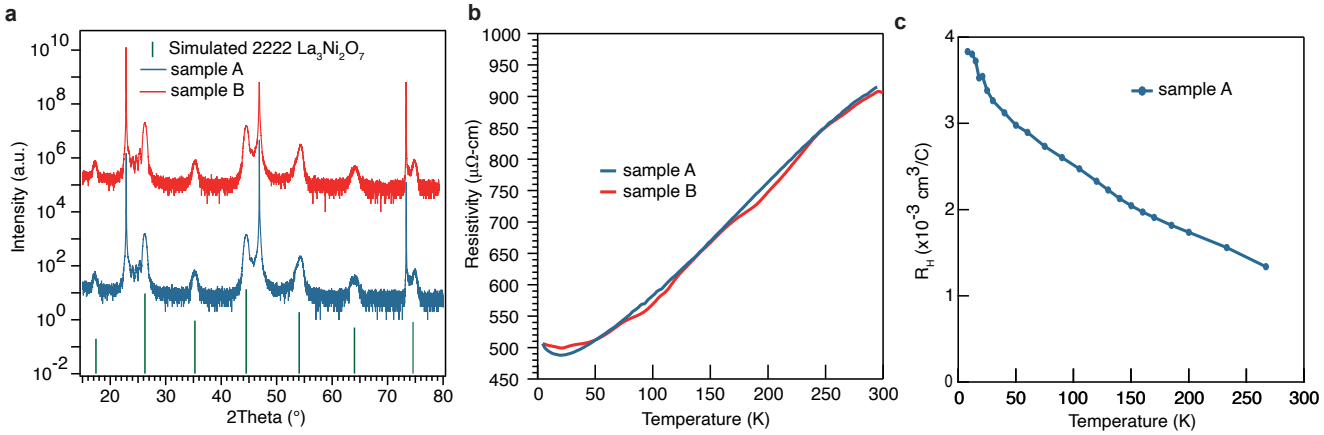

FIG. S1. **A** X-ray diffraction θ-2θ scans of the intensity as a function of scattering angle 2θ for sample A (blue) and B (red) using using Cu $K\alpha_1$ X-rays. Peaks associated with the 16 nm film index to the (0 0 L) Bragg peaks of 2222 $La_3Ni_2O_7$ (green bars). The measurements also exhibit sharp Bragg peaks at 22°, 46° and 72° from the $NdGaO_3$ (110) substrates. Data is offset for clarity. **B** The resistivity of sample A and B vs temperature. The samples have resistivity that is similar in magnitude between the two samples. No clear anomalies the resistivity close to the SDW onset temperature are observed. **C** The Hall coefficient, R_H vs. temperature for sample A.

* Corresponding authors: K. M. Shen (kms272@cornell.edu) and D. G. Hawthorn (david.hawthorn@uwaterloo.ca)

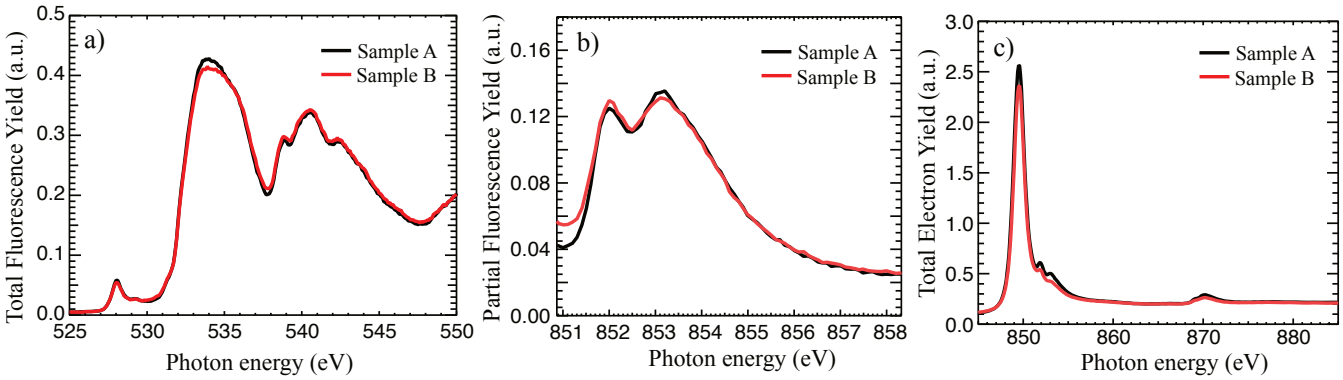

FIG. S2. The x-ray absorption at 21 K of sample A and B at the a) O K edge, measured with total fluorescence yield, b) the Ni L_3 edge measured with partial fluorescence yield and c) the La M_4 (850 eV) and Ni L edges measured with total electron yield.

The x-ray absorption was measured at the O K, La M_4 and Ni L edges as shown in Fig. S2. Sample A and B exhibit similar XAS. At the O K edge, the XAS has a prominent prepeak at 528 eV indicative of holes in O $2p$ states that are hybridized with the Ni $3d$ states. At higher energies, the O K edge XAS results from contributions from both the $La_3Ni_2O_7$ film and the $NdGdO_3$ substrate. In the TEY measurements, the prominent peak at 850 eV is the La M_4 resonance, with the peak at 852 and 853 eV corresponding to the Ni L_3 edge.

II. HARD X-RAY DIFFRACTION

Reciprocal space mapping to characterize the structure of the $La_3Ni_2O_7$ films was performed using hard x-ray diffraction at the QM2 beamline of the Cornell High Energy Synchrotron Source (CHESS). Samples were mounted on a four circle Huber diffractometer in reflection geometry with the sample normal oriented along the ϕ axis. With three different sets of θ $(4, 6, 8$ degrees) and χ $(90, 92, 85$ degrees) rotations, diffraction images were collected on a Pilatus 6M detector using 15 keV incident X-rays while continuously rotating ϕ through 360 degrees in 0.1 degree steps with a 0.1 second counting time per image. Polarization and Lorentz factor corrections were applied to the raw images which were transformed to a 3D reciprocal space map. From these 3D maps, representative measurements shown in figures S3 and S4 were extracted with L values selected to avoid reflections from the NGO substrate. Note: these measurements presented in figures S3 and S4 use H, K and L referenced to the pseudo-tetragonal unit cell depicted in the main text.

L scans through the (1 0 9) and (0 -1 9) structural peaks, shown in figure S3 a and b for sample A and figure S4 a and b for sample B, provide no evidence of a structural phase transition upon lowering the temperature from 300 K to 100 K, below T_{SDW}, although small changes in the Bragg peak intensities are observed for sample A.

This observation is reinforced by the 2D cross-sections of the H - K plane at $L = 4$ and 7, shown in figures S3 and S4 panels c, d, e and f, which show that neither new Bragg peaks nor significant changes in the symmetry of the diffraction patterns are evident between 300 K and 100 K. The measurements do, however, provide evidence of $(\pm 1/2 \ \pm 1/2 \ n)$ (n odd) Bragg peaks.

Notably, these peaks are forbidden in the high pressure Fmmm (Space group 69) structure that is believed to host superconductivity. In the orthorhombic Amam (Space group 63) structure that has been identified in bulk crystals at ambient pressure, (1/2 1/2 n), but not (-1/2 1/2 n) occur.[1] Consequently, the presence of both (1/2 1/2 n) and (-1/2 1/2 n) peaks indicates either the films support twin domains of orthorhombic Amam phase $La_3Ni_2O_7$ or that a new, unreported structure is stabilized via the epitaxial alignment of the lattice to the NGO substrate.

III. POLARIZATION DEPENDENT SCATTERING: MAGNETIC SCATTERING TENSOR

In the vicinity of an x-ray resonance such as the Ni L edge, the resonant elastic x-ray scattering cross-section is given by:[2, 3]

$$I^{\mathrm{cr}}(\boldsymbol{\epsilon}_{\mathrm{in}}, \hbar\omega, \mathbf{Q}) \propto \left| \boldsymbol{\epsilon}^*_{\mathrm{out}} \cdot \left(\sum_j F_j(\hbar\omega, \mathbf{Q}) e^{i\mathbf{Q}\cdot\boldsymbol{r}_j} \right) \cdot \boldsymbol{\epsilon}_{\mathrm{in}} \right|^2 , \tag{S1}$$

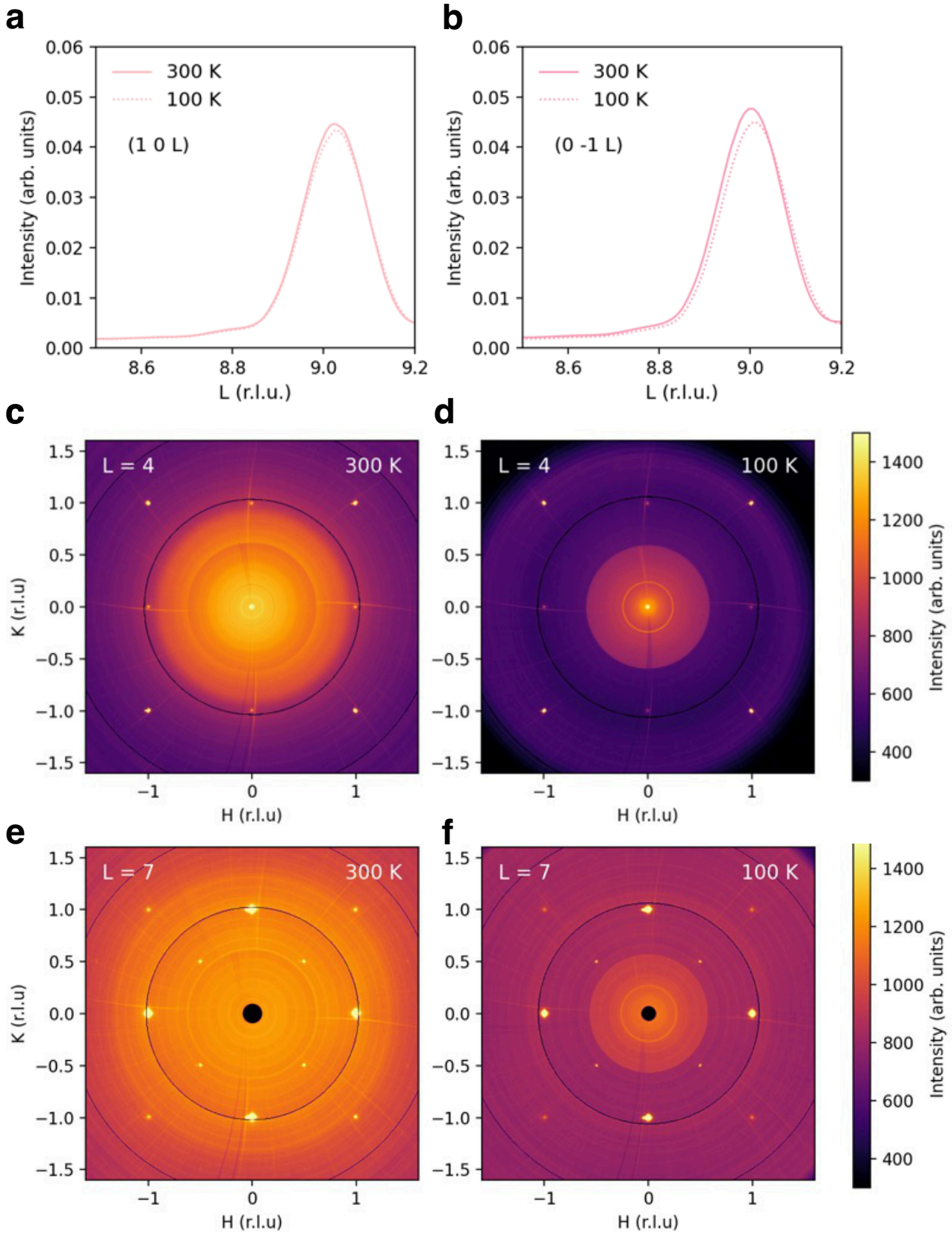

FIG. S3. Hard x-ray reciprocal space mapping for sample A. a) and b) L scans through the (1 0 9) and (0 -1 9) peaks at 300 K and 100 K. c) and d) H - K map of reciprocal space at an even value of L ($L = 4$) at 100 K and 300 K. e) and f) H - K map of reciprocal space at an odd value of L ($L = 7$) at 100 K and 300 K. For odd L, weak peaks at ($\pm 1/2$ $\pm 1/2$ L) are observed that are absent for even L.

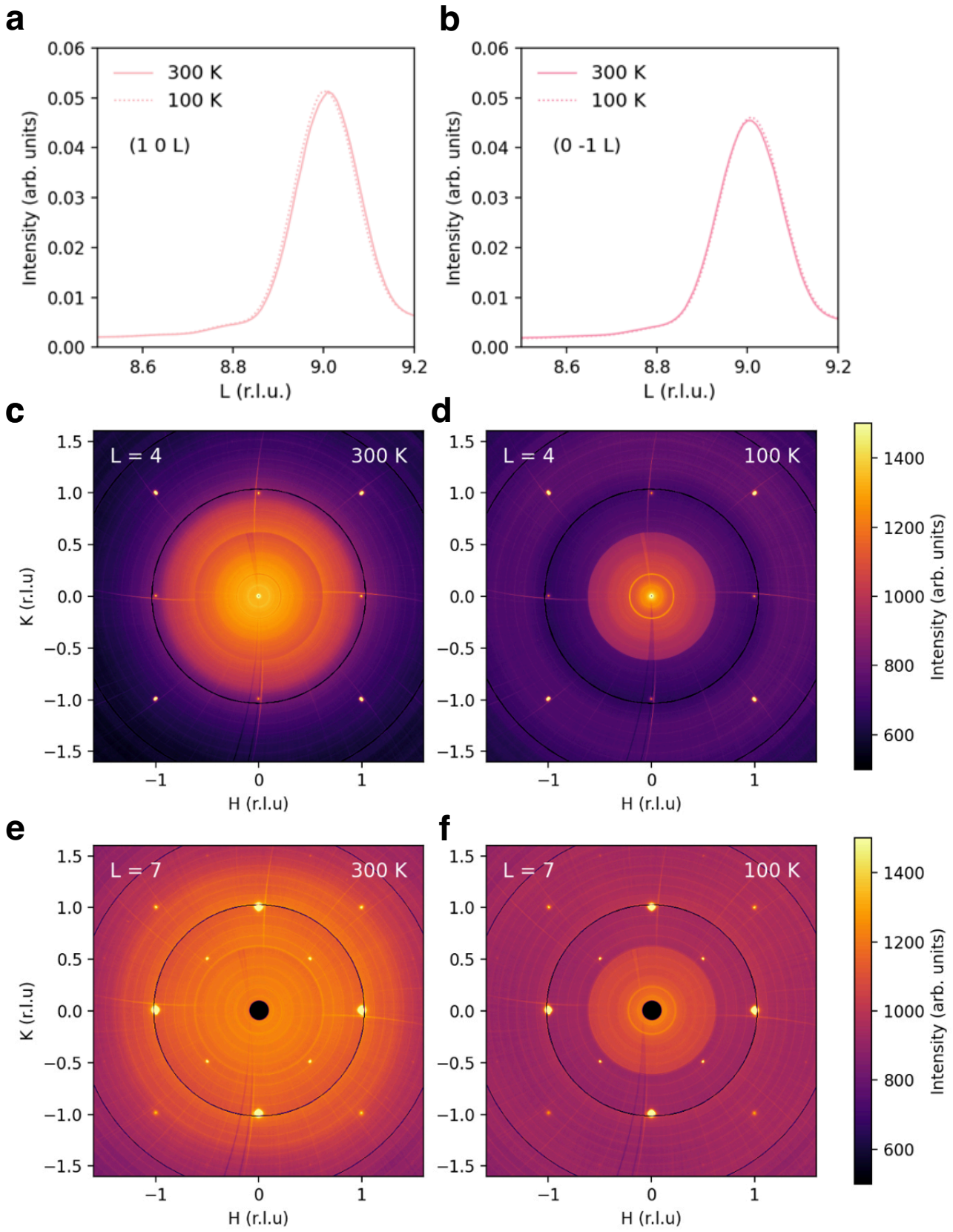

FIG. S4. Hard x-ray reciprocal space mapping for sample B. a) and b) L scans through the (1 0 9) and (0 -1 9) peaks at 300 K and 100 K. c) and d) H - K map of reciprocal space at an even value of L ($L = 4$) at 100 K and 300 K. e) and f) H - K map of reciprocal space at an odd value of L ($L = 7$) at 100 K and 300 K. For odd L, weak peaks at ($\pm 1/2$ $\pm 1/2$ L) are observed that are absent for even L.

where $\hbar\omega$ is the photon energy, $\mathbf{Q} = \mathbf{k}_{\rm out} - \mathbf{k}_{\rm in}$ is the momentum transfer, $\boldsymbol{\epsilon}_{in}$ and $\boldsymbol{\epsilon}_{out}$ are the incident and scattered polarization, respectively. $F_j(\hbar\omega, \mathbf{Q})$ is the photon energy dependent scattering tensor for site j in the lattice:

$$F_j(\hbar\omega) = \begin{bmatrix} F_{j,xx}(\hbar\omega) & F_{j,xy}(\hbar\omega) & F_{j,xz}(\hbar\omega) \\ F_{j,yx}(\hbar\omega) & F_{j,yy}(\hbar\omega) & F_{j,yx}(\hbar\omega) \\ F_{j,zx}(\hbar\omega) & F_{j,zy}(\hbar\omega) & F_{j,zz}(\hbar\omega) \end{bmatrix}. \tag{S2}$$

For a Bragg peak associated with anti-ferromagnetic ordering,

$$\sum_j F_j(\hbar\omega, \mathbf{Q}) e^{i\mathbf{Q}\cdot\boldsymbol{r}_j} = \begin{bmatrix} 0 & \Delta F_z & -\Delta F_y \\ -\Delta F_z & 0 & \Delta F_x \\ \Delta F_y & -\Delta F_x & 0 \end{bmatrix}. \tag{S3}$$

The diagonal components of this tensor are zero and the off-diagonal components associated with the magnetic moment along x, y and z.

Focusing on a single NiO_2 layer, for staggered moments along x, y and z for an (up up down down) colinear magnetic order, the (1/4 1/4 L) magnetic Bragg peak is represented as:

$$\sum_j F_j(\hbar\omega, \mathbf{Q}) e^{i\mathbf{Q}\cdot\boldsymbol{r}_j} = \begin{bmatrix} 0 & F_z^{(1)}(\omega)\Delta m_z & -F_y^{(1)}(\omega)\Delta m_y \\ -F_z^{(1)}(\omega)\Delta m_z & 0 & F_x^{(1)}(\omega)\Delta m_x \\ F_y^{(1)}(\omega)\Delta m_y & -F_x^{(1)}(\omega)\Delta m_x & 0 \end{bmatrix}. \tag{S4}$$

where Δm_u is the staggered moment along $u = x$, y and z and $F_u^{(1)}(\omega)$ is the $k = 1$ component of the expansion of the scattering form factor in spherical harmonics.[3] $F^{(3)}$ terms will also contribute for orthorhombic symmetry, but neglected here for clarity.[3] For the magnetic scattering, this form factor is averaged over lattice planes normal to $\mathbf{Q}$. $F_u^{(1)}(\omega)$ gives the photon energy dependence of resonant scattering and is zero off resonance. If tetragonal or orthorhombic crystal field splitting and spin-orbit coupling are strong effects, $F_x^{(1)}$, $F_y^{(1)}$, and $F_z^{(1)}$ will be in-equivalent and the energy dependence of the scattering will be polarization dependent. However, if these effects are small, the energy dependence of the scattering will have weak sensitivity to the incident photon polarization.

The situation is more complicated for either a spin-charge stripe and/or non-colinear (spiral) order. This introduces 4 sites in the magnetic unit cell, A and B, with $(\mathbf{m}_A, \mathbf{m}_B, -\mathbf{m}_A, -\mathbf{m}_B)$ order. In this instance,

$$\sum_j F_j(\hbar\omega, \mathbf{Q}) e^{i\mathbf{Q}\cdot\boldsymbol{r}_j} = \begin{bmatrix} 0 & F_{A,z}^{(1)}\Delta m_{A,z} + iF_{B,z}^{(1)}\Delta m_{B,z} & -F_{A,y}^{(1)}\Delta m_{A,y} - iF_{B,y}^{(1)}\Delta m_{B,y} \\ -F_{Az}^{(1)}\Delta m_{Az} - iF_{B,z}^{(1)}\Delta m_{B,z} & 0 & F_{A,x}^{(1)}\Delta m_{A,x} + iF_{B,x}^{(1)}\Delta m_{B,x} \\ F_{A,y}^{(1)}\Delta m_{A,y} + iF_{By}^{(1)}\Delta m_{B,y} & -F_{A,x}^{(1)}\Delta m_{A,x} - iF_{B,x}^{(1)}\Delta m_{B,x} & 0 \end{bmatrix} \tag{S5}$$

Charge order or bond-disproportionation will generally lead to a different energy dependence of $F_{A,u}^{(1)}(\omega)$ and $F_{B,u}^{(1)}(\omega)$, and as is the case with bond-disproportionation in $RENiO_3$ staggered moments with different amplitudes and preferred orientations ($\Delta\mathbf{m}_A \neq \Delta\mathbf{m}_B$). Unless $\Delta\mathbf{m}_A$ and $\Delta\mathbf{m}_B$ are colinear, this also leads to energy dependence of the scattering being dependent on photon polarization, even if $F_x^{(1)}(\omega) \simeq F_y^{(1)}(\omega) \simeq F_z^{(1)}(\omega)$.

Finally, non-colinear order without charge order or bond-disproportionation, would have $F_{A,u}^{(1)}(\omega) = F_{B,u}^{(1)}(\omega)$, but $\Delta\mathbf{m}_A \neq \Delta\mathbf{m}_B$.

A. Measuring the Scattering Tensor Components

To measure the symmetry of the scattering tensor S4, scattering tensor may be rotated relative to the incident and scattered photon polarization.[3, 4] With the photon polarization in the laboratory reference frame (denoted by the subscript ℓ) Eq. S1 can be expressed as

$$I^{cr}(\boldsymbol{\epsilon}_{in}, \hbar\omega, \mathbf{Q}) \propto \left| \boldsymbol{\epsilon}_{out,\ell}^* \cdot R \left(\sum_j F_j(\hbar\omega, \mathbf{Q}) e^{i\mathbf{Q}\cdot\boldsymbol{r}_j} \right) R^\top \cdot \boldsymbol{\epsilon}_{in,\ell} \right|^2, \tag{S6}$$

where R is a rotation matrix that rotates the sample into the geometry necessary to satisfy the Bragg condition for a photon energy $\hbar\omega$ and momentum transfer $\mathbf{Q}$. The rotation matrix R can also rotate the sample azimuthally about $\mathbf{Q}$ by an angle ϕ, as depicted in Fig. 2a of the main text.

For the sample not mounted on the wedge with $\phi = 0$, such as measurements of the (1/4 1/4 L) and ($-1/4$ $-1/4$ L) peaks or peaks at different L values, give

$$I^{cr}(\pi, \phi = 0) = |\Delta F_{-110} \sin\Omega|^2 + |\Delta F_{110} \cos\theta - \Delta F_{001} \sin\theta|^2, \tag{S7}$$

and

$$I^{cr}(\sigma, \phi = 0) = |\Delta F_{110} \cos(\theta - \Omega) - \Delta F_{001} \sin(\theta - \Omega)|^2, \tag{S8}$$

where Ω is the angle of the scattered beam relative to the incident beam.

The weak scattering with σ versus π at $\phi = 0$ for the (1/4 1/4 L) and ($-1/4$ $-1/4$ L) peaks at various L values and photon energies, which have different values of θ and Ω, can easily understood from equations S7 and S8 if $\Delta F_{-110} >> \Delta F_{110}$ and $\Delta F_{-110} >> \Delta F_{001}$. This, along with the azimuthal angle dependent measurements, provide strong constraints on the orientation of the staggered moment at low T as being in the NiO plane and perpendicular to $\mathbf{Q}_{SDW}$.

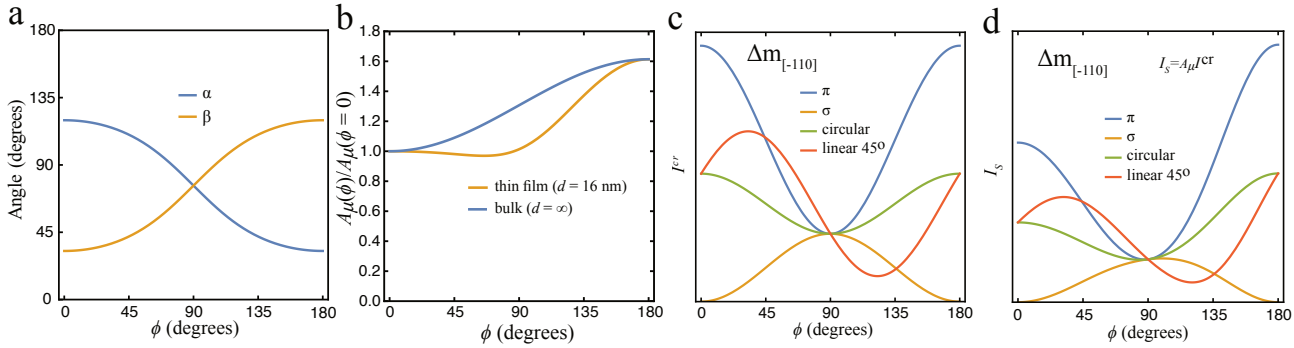

FIG. S5. For the measurement geometry shown in figure 2 of the main text ($\Omega = 2\theta = 152.4°$ and $\theta_w = 43.7°$) a) The angle of incidence α and scattering β versus ϕ b) The absorption correction, A_μ defined in eqn. S10. c) The calculated scattering cross-section, I^{cr} for $\Delta m_{[-110]}$. d) The calculating scattering intensity, $I_s = I^{cr} A_\mu$, including the absorption correction, for $\Delta m_{[-110]}$.

B. Absorption correction

While equation S1 provides the expression for the scattering cross-section, the measured intensity is influenced by the absorption of the incident and scattered photons.[4] For an absorption co-efficient that is approximately isotropic, having weak linear or circular dichroism, the absorption co-efficient, $\mu(\omega)$ is taken as being independent of photon polarization. The resulting scattering intensity, I_s is proportional to the scattering cross-section, I^{cr}, multiplied by an absorption factor, $A_\mu(\alpha, \beta)$, that depends on the angles of the incident (α) and scattered (β) x-rays with the surface of the sample (small α corresponds to grazing incidence).

For a thin film sample of thickness, d, $A_\mu(\alpha, \beta)$ is given by:

$$A_\mu(\alpha, \beta) = \int_0^d \frac{1}{\sin\alpha} e^{-\mu z/\sin\alpha} e^{-\mu z/\sin\beta} dz \tag{S9}$$

$$= \frac{1 - e^{-d\mu(\csc\alpha + \csc\beta)}}{\mu\left(1 + \frac{\sin\alpha}{\sin\beta}\right)}, \tag{S10}$$

where z is the depth into the sample.

For our samples, the film thickness is $d = 16$ nm. μ is estimated using Ni L_3 absorption spectra on $NdNiO_3$ from ref.[5], which has a lineshape similar to our $La_3Ni_2O_7$ spectra. The spectra is then scaled and offset to match the

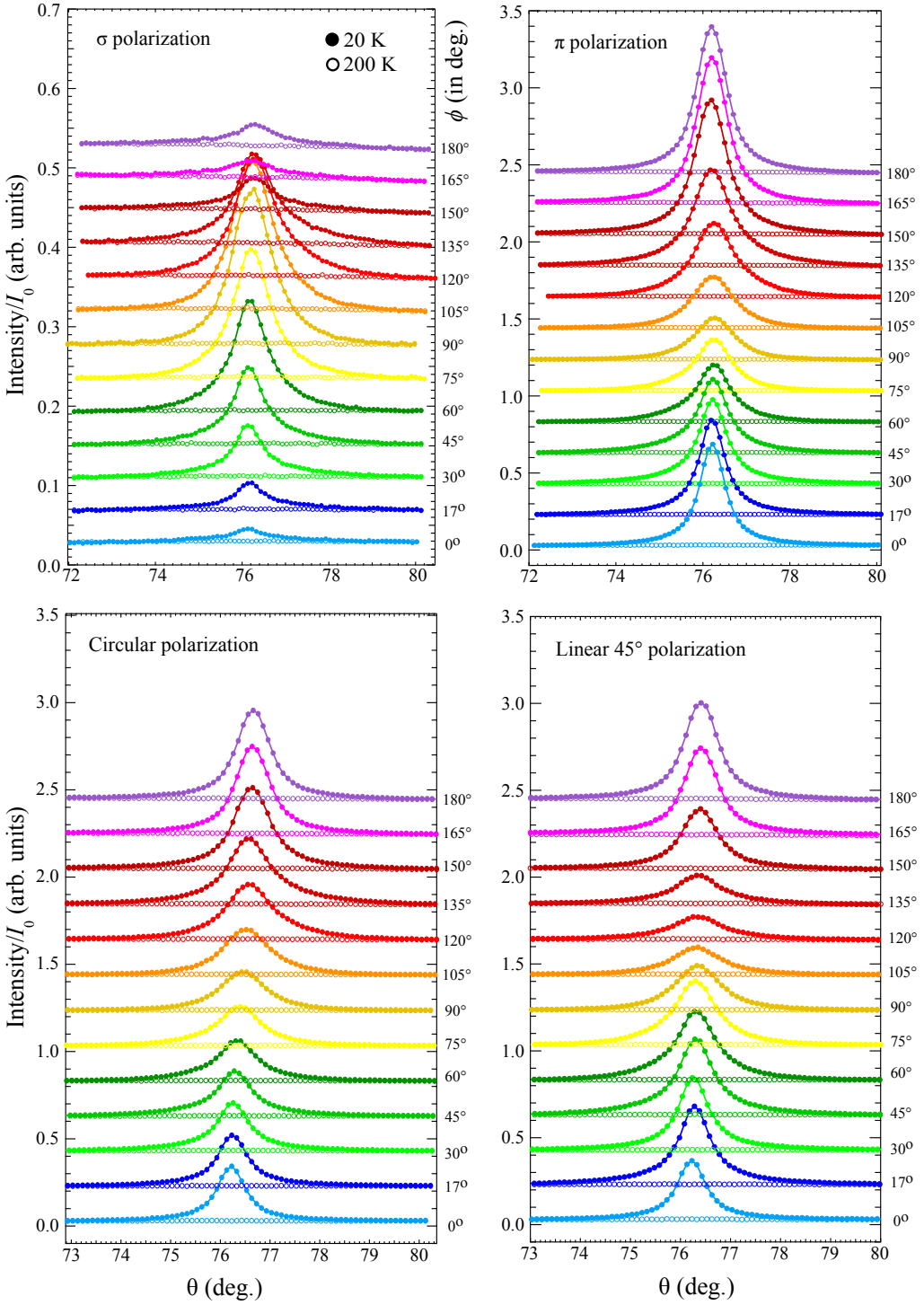

FIG. S6. a) Raw measured intensity through the (1/4 1/4 1.91) SDW peak as a function of sample angle, θ, polarization and azimuthal angle, ϕ, as defined in figure 2a of the main text. Measurements are taken at the Ni L_3 edge (852 eV) at 20 K (closed circles) and 200 K (open circles) and normalized to the incident beam intensity I_0. Measurements at different ϕ values are offset for clarity.

absorption tabulated by NIST to be above and below the edge.[6] Using this procedure, we estimate that $\mu(852\text{eV}) = 19 \times 10^{-3}$ nm^{-1} and $\mu(870\text{eV}) = 12 \times 10^{-3}$ nm^{-1}.

α and β depend on the sample angles θ and ϕ depicted in figure 2a of the main text, as well as the detector angle Ω. This results in a changes in peak intensity with ϕ during azimuthal scans, as depicted in figure S5. It also impacts

the measured intensity as a function of L, owing to the large changes in α and β involved in scanning the (1/4 1/4) peak from $L = 1.5$ to 2.1.

The calculated scattering intensity as a function of ϕ shown in figure 2c and 2g of the main text is the absorption cross-section from Eqn.'s 1 and 2 of the main text, multiplied by Eqn. S10: $I_s \propto I^{cr} A_\mu$.

IV. AZIMUTHAL ANGLE DEPENDENCE OF THE (1/4 1/4 L) PEAK INTENSITY

The total intensity includes the scattering intensity, I_s, from the SDW peak and a temperature independent background from x-ray fluorescence. The scattering intensity, I_s shown in figure 2b of the main text is found by subtracting the background fluorescence measured above T_{SDW} (200 K) data from the total intensity (scattering + background fluorescence) measured at 20 K. In Fig. S6 we show the raw total intensity at the Ni L_3 edge (852 eV), normalized to the incident beam intensity I_0, as a function of ϕ, θ and incident photon polarization at 20 K and 200 K.

V. MEASUREMENTS OF THE (1/4 1/4 L) SDW PEAK IN SAMPLE B

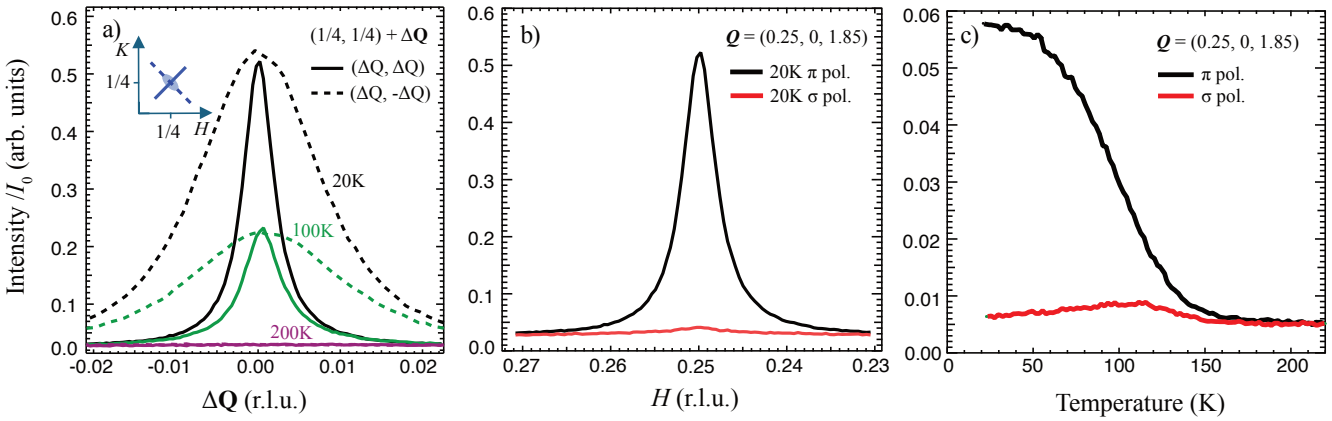

FIG. S7. **The (1/4 1/4 1.85) SDW peak in sample B measured at the Ni L_3 edge (852 eV).** a) Cuts though the (1/4 1/4) Bragg peak parallel and perpendicular to $\mathbf{Q}_{SDW}$. b) Measured intensity with σ and π incident x-rays showing strong linear dichroism. c) The temperature dependence of the intensity at the (1/4 1/4 1.85) peak with σ and π incident light. Note for this temperature dependence measurement, a different detector (multichannel plate) was used instead of the detector (silicon drift detector) used in panels a and b.

Measurements were performed on a 2nd sample, sample B, with similar properties to sample A. As shown in figure S7a, the peak is anisotropic, with a broader peak shape perpendicular to $\mathbf{Q}_{SDW}$ than parallel to $\mathbf{Q}_{SDW}$. Sample B has a slightly weaker and broader SDW peak of sample A at 20 K, with a peak amplitude of 2/3 that of sample A and correlation length $\xi_{\|} = 200$ Å. As shown in figure S7b, sample B exhibits the same strong linear dichroism to the SDW peak at low T, with scattering much stronger with π incident polarization versus σ incident polarization, suggesting a common low T magnetic configuration between the two samples. In addition, as shown in figure S7c, sample B exhibit the non-monotonic T dependence for scattering with σ incident light, an observation we attribute an increase in domain wall density with increasing temperature. While qualitatively similar, sample B has an SDW onset temperature T_{SDW} that is approximately 10 K lower than sample A.

The L dependence of the SDW peak, described in the next section, was mapped out in sample B.

VI. L DEPENDENCE

The inter-layer coupling and c-axis correlation length of the SDW order can be deduced from the L dependence of the structure factor, I_L. In order to determine I_L, the measured scattering intensity, I_s vs. L is first determined by subtracting the fluorescent background measured 220 K (above T_{SDW}) from the total intensity (scattering + fluorescent background) at 20 K, as shown in figure S8 a and S9 a).

Then I_L is found by correcting I_s for the variations in both the scattering cross-section, I^{cr}, of the (1/4 1/4) and (-1/4 -1/4) peaks, and the absorption of the incident and scattered light, A_μ, that occur due to changes in the measurement geometry as L is increased. For instance, as shown in fig S8 b) and d), for the (1/4 1/4 L) peak at 870 eV, the angles α (equal to ω for this scattering geometry), β and the detector angle, Ω, all vary significantly with L. This leads to variation in A_μ (from eqn. S10 and I_{cr} (calculated from eqn. S7 assuming the staggered moments are perpendicular to $\mathbf{Q}_{SDW}$ and are in the NiO_2 planes), as depicted in figure S8 c. I_L is determined by

$$I_L = \frac{I_s}{A_\mu \times I^{cr}_{(\pm 1/4, \pm 1/4)}}. \tag{S11}$$

As shown in figure S8 d, after applying these corrections, I_L = is peaked at $L = 2$ and is minimal at $L = 1.5$. Similar corrections on measurements of the (-1/4 -1/4 L) peak and at the L_3 edge, which spans a lower range of L, are shown in figure S9 b). Despite significant variation in their I_s (figure S9 a), very similar L dependence of I_L, providing confidence in the correction procedure.

This L dependence can be fit to possible 3D coupling between layers. We consider 4 possibilities, with anti-ferromagnetic or ferromagnetic intra and inter bilayer coupling. Notably FM inter bilayer and AFM intra bilayer coupling or AFM inter bilayer and FM intra bilayer coupling have a zero in the structure factor at $L = 2$, inconsistent with our measurement.

The L dependence of the structure factor for the two other possibilities, depicted in figure S9 d and e, is $S_{FM}(L) \propto (1 + e^{i2\pi L z_{bilayer}})(1 + e^{i\pi L})$ and $S_{AFM}(L) \propto (1 - e^{i2\pi L z_{bilayer}})(1 + e^{i\pi L})$.

The structure factor models were fit by multiplying $S_{FM}(L)$ or $S_{AFM}(L)$ with a Lorentzian to account for a short correlation length along the c axis. Both of these models provide reasonable fits the measurements, as shown in figure S9 c). A single Lorentzian without an L dependent structure factor also provides an adequate fit to the data.

Although we are unable to distinguish between FM and AFM interlayer coupling based on these measurements, Chen et al. [7] identified AFM interlayer intra bilayer exchange interactions from the RIXS measurements, favouring the AFM structure depicted in figure S9 d).

VII. SCATTERING INTENSITY AND PEAK WIDTH WITH σ INCIDENT POLARIZATION

In figure S10 a, (H, H) scans of the total measured intensity (scattering + fluorescence) through (H H 1.93) peak are shown is shown at various temperatures. The scattering intensity with σ incident polarization, I_S, shown in figure 4 of the main text was determined subtracting the background at 220 K, above the SDW onset temperature from the total intensity at lower temperature $I_S(T) = I(T) - I(220K)$.

For $T > 120$ K, the scattering can be fit to a Lorentzian with a peak width that is greater than the peak width measured with π incident polarization. However, at low temperature, a single Lorentzian does not fit well to the data. Rather, at 20 K, (figure S10 b) the scattering exhibits a two-component peak: a broad peak, with a width comparable to the peak width measured with σ polarization at higher temperature, and a narrow peak, with a width comparable to the peak width measured with π incident polarization at 20 K.

Considering this, we fit I_S with σ polarization as a function of temperature to two Lorentzians, one with a broad peak and one with a narrow peak, as well as a constant offset, as shown in figure S10 b-f). For these fits, the peak width for the narrow peak (green) is constrained to be equal to the peak width measured with π incident polarization and both peak were constrained to have the same peak wavevector. This shows the intensity of the broad peak to increase with increasing temperature, whereas the intensity of the narrow peak to decreases with increasing temperature, eventually becoming unresolved by the fits at 150 K. The resulting width of the broad peak (red), given in figure 4d of the main text, is weakly temperature dependent below 150 K.

We attribute a significant part of the narrow peak to an artifact of having the incident beam with nominal σ incident photon polarization contain a small faction of light with π incident polarization. The σ incident polarization is generated by an elliptically polarized undulator (EPU) in the synchrotron storage ring, whose magnets are controlled to generate a specified nominal incident polarization. However, in addition to light from the EPU, a small fraction, ρ of order 1% of the total beam intensity is π polarized light originating from dipole and chicane magnets in the storage ring. Thus, the beam intensity with nominal incident polarization $\boldsymbol{\epsilon}_{in}$ is actually $I_{\boldsymbol{\epsilon}_{in},nominal} = (1-\rho)I_{\boldsymbol{\epsilon}_{in}} + \rho I_\pi$. This additional source of π incident light becomes relevant when there is a large dichroism between π and σ scattering ($I_{S,pi} >> I_{S,sigma}$), as is the case here at low temperature with $\phi = 0$.

Comparing the fitted amplitude of the narrow peak with nominal σ polarization light at 20 K to the scattering intensity with π incident light, $I_\pi(20K)$ gives an intensity ratio $I_\pi(20K)/I_{\sigma,nominal}(20K) = 0.015$ (figure S10 b). This is consistent with expected values of ρ (of order 1%) for the beamline, suggesting the narrow peak may be entirely an

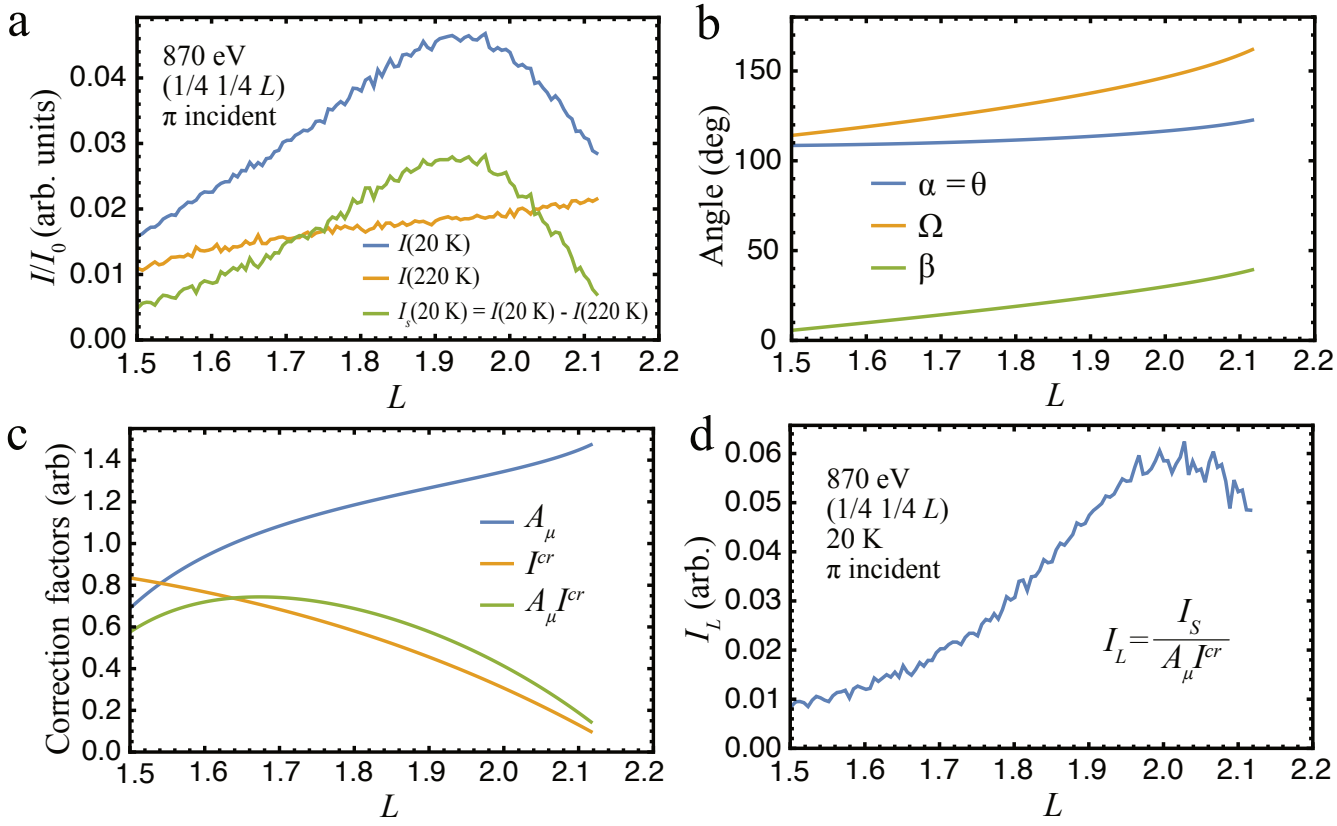

FIG. S8. L **dependence of the (1/4 1/4 L) SDW peak at the Ni L_2 edge, 870 eV and π incident polarization.** a) The measured intensity at 20 K, I which measures scattering plus background fluorescence, and 220 K, which is only background fluorescence. The subtraction of 20 K and 220 K is the scattering intensity I_s at 20 K from the SDW Bragg peak. Data is normalized by the incident x-ray intensity I_0. b) The angles, $\alpha = \theta$, β and Ω vs. L. c) The calculated correction factors from absorption (Eqn. S10) and the angle dependence of the in-plane (1/4 1/4) peak scattering cross-section, I^{cr}). c) The L dependence of the scattering cross-section, I_L, given by eqn. S11. I_L reveals the L dependence of the structure factor, showing it to be peaked at $L = 2$ and small at $L = 1.5$.

artifact of the impure polarization. However, since the precise value of ρ was not characterized under the conditions used in the beamtime, it is possible that a portion of the narrow peak intensity is intrinsic, resulting from σ scattering.

[1] H. Sun, M. Huo, X. Hu, J. Li, Z. Liu, Y. Han, L. Tang, Z. Mao, P. Yang, B. Wang, J. Cheng, D.-X. Yao, G.-M. Zhang, and M. Wang, Signatures of superconductivity near 80 K in a nickelate under high pressure, Nature **621**, 493 (2023).

[2] J. Fink, E. Schierle, E. Weschke, and J. Geck, Resonant elastic soft x-ray scattering, Reports on Progress in Physics **76**, 056502 (2013).

[3] M. W. Haverkort, N. Hollmann, I. P. Krug, and A. Tanaka, Symmetry analysis of magneto-optical effects: The case of x-ray diffraction and x-ray absorption at the transition metal $L_{2,3}$ edge, Phys. Rev. B **82**, 094403 (2010).

[4] A. J. Achkar, F. He, R. Sutarto, C. McMahon, M. Zwiebler, M. Hucker, G. D. Gu, R. Liang, D. A. Bonn, W. N. Hardy, J. Geck, and D. G. Hawthorn, Orbital symmetry of charge-density-wave order in $La_{1.875}Ba_{0.125}CuO_4$ and $YBa_2Cu_3O_{6.67}$, Nature Materials **15**, 616 (2016).

[5] C. T. Parzyck, N. K. Gupta, Y. Wu, V. Anil, L. Bhatt, M. Bouliane, R. Gong, B. Z. Gregory, A. Luo, R. Sutarto, F. He, Y.-D. Chuang, T. Zhou, G. Herranz, L. F. Kourkoutis, A. Singer, D. G. Schlom, D. G. Hawthorn, and K. M. Shen, Absence of $3a_0$ charge density wave order in the infinite-layer nickelate $NdNiO_2$, Nature Materials **23**, 486 (2024).

[6] C. Chantler, Detailed tabulation of atomic form factors, photoelectric absorption and scattering cross section, and mass attenuation coefficients in the vicinity of absorption edges in the soft x-ray(z=30-36, z=60-89, e=0.1 kev-10 kev), addressing convergence issues of earlier work., J. Phys. Chem. Ref. Data **29**, 597 (2000).

[7] X. Chen, J. Choi, Z. Jiang, J. Mei, K. Jiang, J. Li, S. Agrestini, M. Garcia-Fernandez, X. Huang, H. Sun, D. Shen, M. Wang, J. Hu, Y. Lu, K.-J. Zhou, and D. Feng, Electronic and magnetic excitations in $La_3Ni_2O_7$, Nat. Comm. **15**, 9597 (2024).

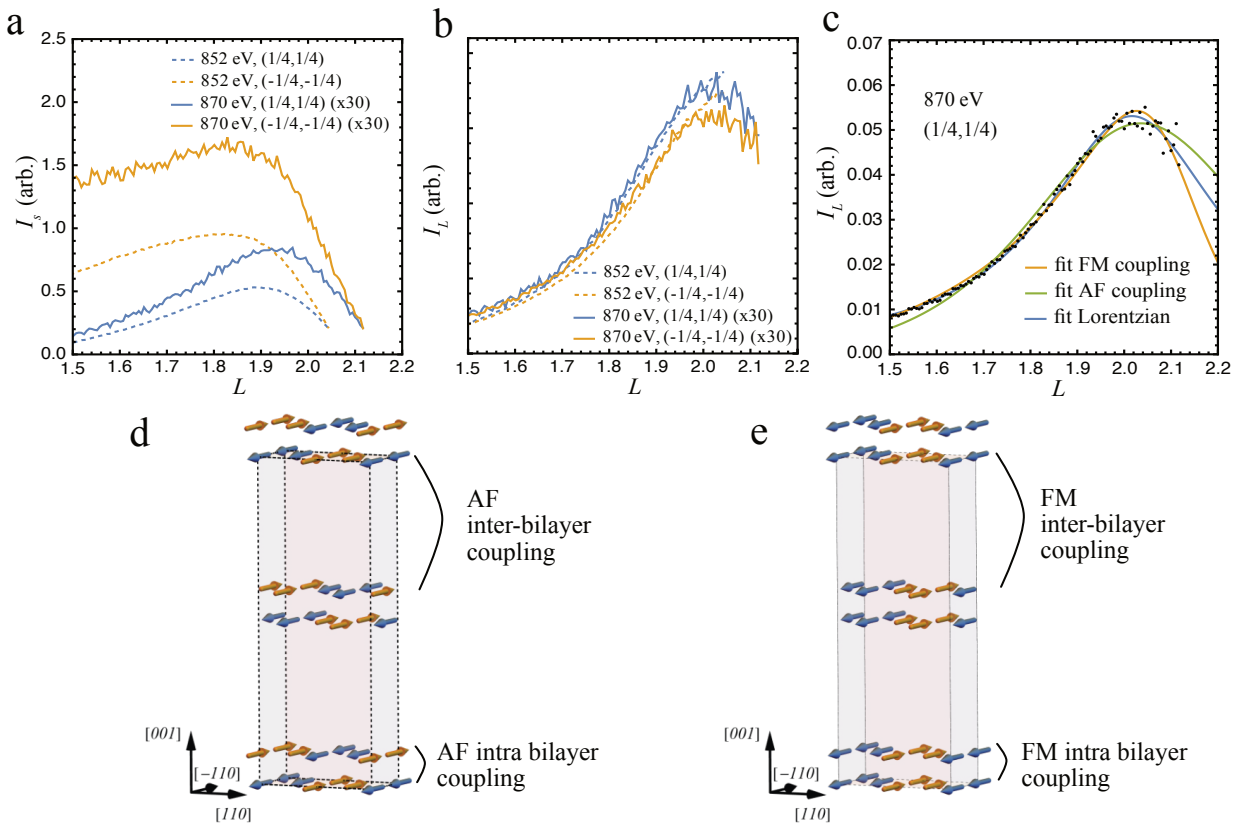

FIG. S9. a) The measured scattering intensity, I_s, at 20 K for the (1/4 1/4 L) and (-1/4 -1/4 L) SDW peaks at the Ni L_3 (852 eV) and L_2 (870 eV) energies. b) The L dependence of the SDW structure factor, I_L, corrected for absorption, A_μ, and the angle dependent (1/4 1/4) scattering cross-section, I_{cr}. c) Fits I_L at 870 eV for a single Lorentzian (blue), a model with ferromagnetic bilayer coupling and ferromagnetic interlayer coupling (orange), and a model with antiferromagnetic bilayer coupling and antiferromagnetic inter-layer coupling (green). d) and e) Models of the 3D magnetic structure with antiferromagnetic or ferromagnetic inter-layer couplings that are consistent with the L dependence of I_L.

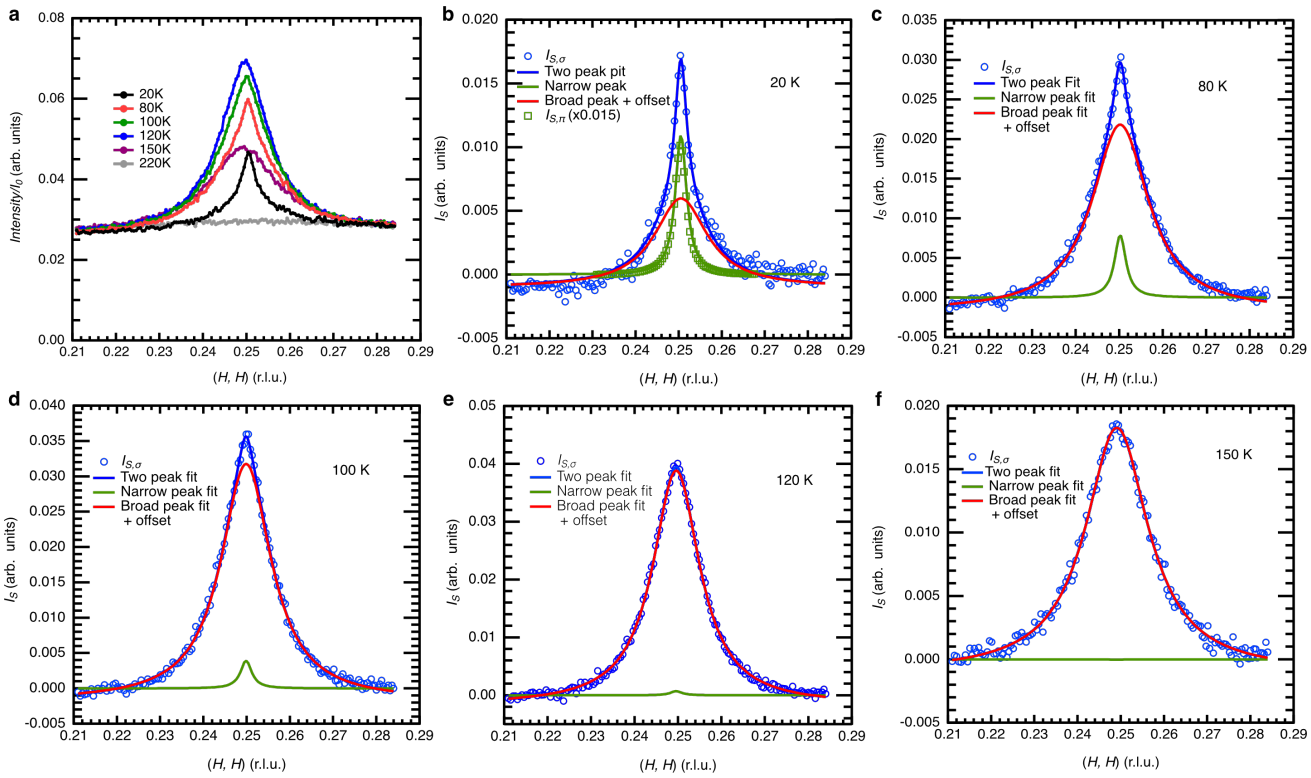

FIG. S10. a) Scans through (H, H, 1.93) of the total measured intensity normalized to the incident beam intensity, I/I_0, at various temperatures with nominal σ incident polarization light at the Ni L_3 (852 eV). The scattering intensity, $I_{S,\sigma}(T) = I(T) - I(220\text{ K})$ at various temperatures is plotted in panels b) though f) along with two peak fits to the peak (blue line). These fits include a narrow peak (green) that is constrained to have the same width as the peak width measured with π incident light, as well as a broad peak and a constant offset (red). In b) the measured scattering intensity at 20 K with π incident light scaled by a factor of 0.015 (green squares) is also shown.